ACS APPLIED MATERIALS & INTERFACES

www.acsami.org

Research Article

Thiazoline Carbene–Cu(I)–Amide complexes: Efficient White Electroluminescence from Combined Monomer and Excimer Emission

Armands Ruduss, Baiba Turovska, Sergey Belyakov, Kitija A. Stucere, Aivars Vembris, Glib Baryshnikov, Hans Ågren, Jhao-Cheng Lu, Wei-Han Lin, Chih-Hao Chang,* and Kaspars Traskovskis*

Cite This: *ACS Appl. Mater. Interfaces* 2022, 14, 15478–15493

Read Online

ACCESS | Metrics & More | Article Recommendations | Supporting Information

ABSTRACT: Luminescent carbene–metal–amide complexes bearing group 11 metals (Cu, Ag, Au) have recently attracted great attention due to their exceptional emission efficiency and high radiative decay rates (k_r). These materials provide a less costly alternative to organic light-emitting diode (OLED) emitters based on more scarce metals, such as Ir and Pt. Herein, a series of eight Cu(I) complexes bearing as yet unexplored 1,3-thiazoline carbenes have been investigated and analyzed with respect to their light emission properties and OLED application. For the first time among the class of copper-based organometallic compounds the formation of efficient electroluminescent excimers is demonstrated. The prevalence of electroluminescence (EL) from either the monomer (bluish green) or the excimer (orange-red) can be adjusted in vacuum-deposited emissive layers by altering the extent of steric encumbrance of the emitter or its concentration. Optimized conditions in terms of the emitter structure and mass fraction allowed a simultaneous EL from the monomer and excimer, which laid the basis for a preparation of a single-emitter white OLED (WOLED) with external quantum efficiency of 16.5% and a maximum luminance of over 40000 cd m^{-2}. Wide overlapping emission bands of the monomer and excimer ensure a device color rendering index (CRI) of above 80. In such a way the prospects of copper complexes as cost-effective materials for lighting devices are demonstrated, offering expense reduction through a cheaper emissive component and a simplified device architecture.

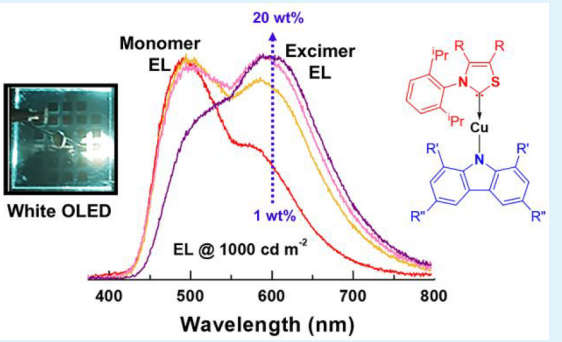

KEYWORDS: *thermally activated delayed fluorescence, copper complex, organic light-emitting diode, carbene–metal–amide, excimer, Marcus theory, conformational locking, white emission*

INTRODUCTION

Advancements in organic light-emitting diode (OLED) technology has aided the rise of innovative consumer-grade products, such as mobile devices and TV displays with unmatched power consumption characteristics, form factors, refresh rates and image quality.[1] In addition, great attention has recently been devoted to the development of white OLEDs (WOLEDs) for next-generation lighting devices.[2] Emitters with suitable photophysical properties play a crucial role in attaining the desired efficiency and longevity parameters of these devices. Due to the intrinsic nature of electronic excitations, which generate singlet (S) and triplet (T) excitons in a 25%:75% ratio, the ability to ensure emission by circumventing the forbidden nature of the $T_1 \rightarrow S_0$ transition is the main requirement for efficient emitters.[3] Organometallic transition-metal complexes bearing Ir, Pt, Os, and Re atoms possess strong spin–orbit coupling (SOC), allowing fast phosphorescence with radiative rates (k_r) in the range of 10^5–10^6 s^{-1}.[4−6] Although these materials have experienced the most widespread practical use, the rarity and high cost of the mentioned elements have fueled research interest in compounds that feature more abundant metals.[7,8] Particularly, Cu complexes have attracted attention due to the absence of efficiency-reducing d → d* transitions in the d^{10}-configured outer electron shell.[9−13] While Cu does not promote a rapid emission directly from the T_1 state due to insufficient SOC strength, the presence of this heavy atom aids in efficient and fast triplet state harvesting through a thermally activated delayed fluorescence (TADF) mechanism.[14] The early structural examples of such compounds mostly possessed metal to ligand charge transfer (MLCT) states. Due to the formal oxidation of the metal center upon photoexcitation, the

Received: January 14, 2022
Accepted: March 15, 2022
Published: March 29, 2022

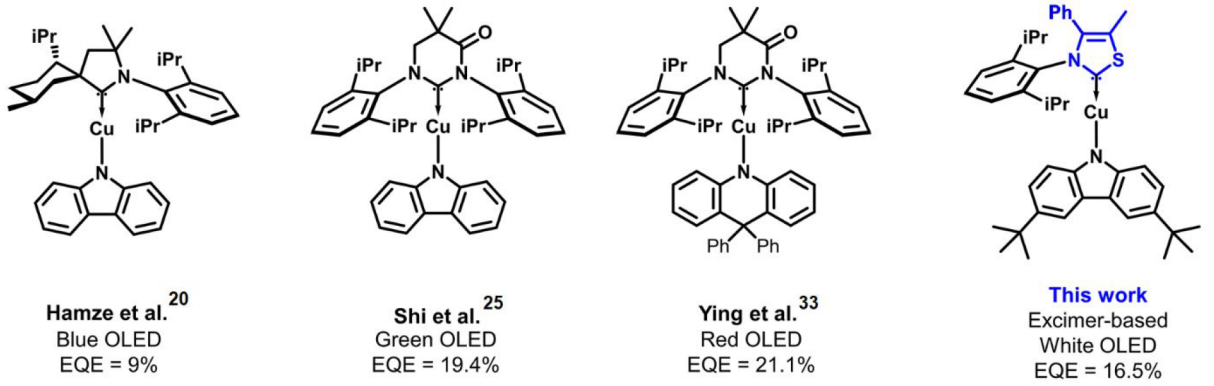

Figure 1. Known Cu(I)-based CMA emitters with a demonstrated OLED use.

Scheme 1. Synthesis of CMA Emitters 1−8

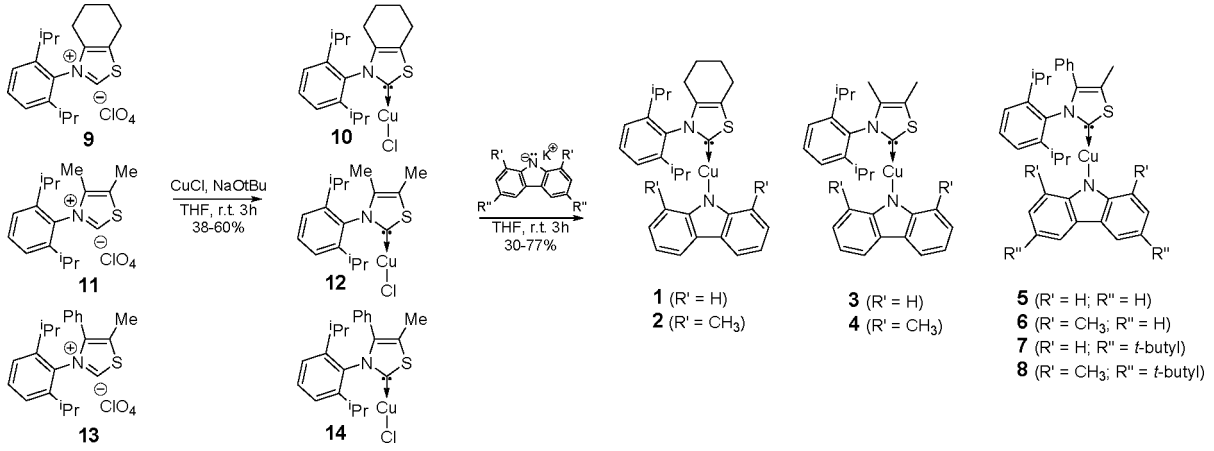

geometry of these complexes transforms, so reducing the attainable photoluminescence quantum yield (Φ_{PL}).[15,16]

Recently a new class of highly emissive d^{10}-element (Cu, Ag, Au)-based emitters have emerged in the form of two-coordinate linear geometry complexes. Composed of metal-bound electrophilic carbene and electron-rich amide ligands, these compounds are often referred to as "carbene−metal−amides" (CMAs).[17−20] The TADF emission in these complexes predominantly originates from ligand to ligand charge transfer (LLCT) states, and Φ_{PL} values of up to 1.0 can be attained due to the limited metal involvement. Spatial separation of the highest occupied and lowest unoccupied molecular orbitals (HOMO and LUMO) ensures that the energy gap between the lowest energy S and T states (ΔE_{ST}) is small, resulting in fast direct and reverse intersystem crossing rates (k_{ISC} and k_{RISC}) and allowing TADF lifetimes of below 1.0 μs.[21−24] In addition to systematically tunable emission color, covering the visible spectrum,[25−29] these compounds show characteristics and OLED performance that are comparable to those of state of the art Ir and Pt emitters.[19,25]

Structure−property relations for this compound class have been well established. Emission lifetimes (τ) become shorter in the sequence Cu, Au, and Ag, partially in relation to the ΔE_{ST} values of the corresponding complexes.[21] The structure of the ligands mainly influences the emission wavelength. The electron-donating amide determines the HOMO energy level of the emitter, which can be modified with an introduction of electron-accepting or -donating structural fragments.[25,30] All of the known strongly emissive CMAs feature carbenes with an electrophilic nature.[27,31] In particular, cyclic alkyl amino carbenes (CAAC),[19,32] monoamido and diamido carbenes (MAC, DAC),[25,33] and aryl-fused carbenes[27,34,35] have been successfully used to synthesize such emitters. Despite these examples the structural diversity of CMAs is still rather low due to the small number of accessible carbenes that can provide emitters with a combination of high emission efficiency and chemical stability. Particularly, this can be addressed to the emitters based on the more abundant Cu atom, for which only a small number of reports have demonstrated a practical OLED use (Figure 1).

Here we investigate the novel structures of highly luminescent CMAs, which contain an as yet unexplored 1,3-thiazoline carbene fragment. A series of complex molecules **1−8** was synthesized by altering the substituents at the 4- or 5-position of either the 1,3-thiazoline carbene or the carbazole amide (Scheme 1). In doped PMMA films the compounds possess high Φ_{PL} values (0.71−0.86) with radiative rates in the range k_r = (2.8−7.2) × 10^5 s^{-1}. As we show, the emissive rates of the complexes can be substantially increased by the simultaneous introduction of sterically demanding groups at both the thiazoline carbene 4-position and the carbazolide 1,8-positions. The results of X-ray structural analyses and DFT calculations relate this effect to a conformational locking that limits the degree of torsional motion of the carbazolide ligand. On the basis of the investigated compounds, for the first time among the class of Cu(I) emitters we demonstrate the formation of efficient electroluminescent excimers. The formation of emissive dimers is related to the favorable molecular structure of 1,3-thiazoline-

https://doi.org/10.1021/acsami.2c00847
ACS Appl. Mater. Interfaces 2022, 14, 15478−15493

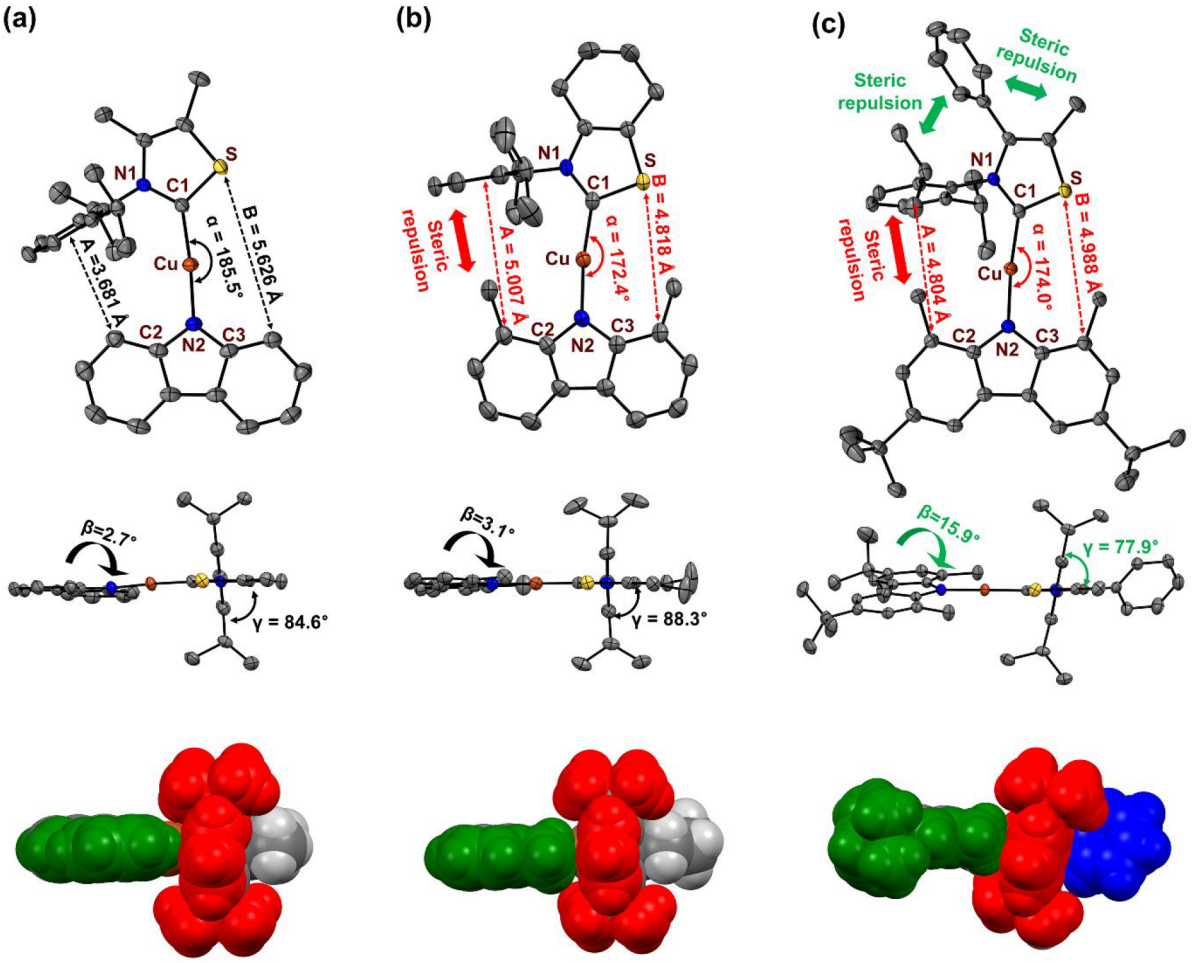

Figure 2. Top and side views of X-ray structures for **3** (a), **2** (b) and **8** (c). Ellipsoids are shown at 50% probability level. Hydrogen atoms are removed for clarity. Definitions: *A*, distance between the carbon at the carbazolide 1-position and the Dipp centroid; *B*, distance between the carbon at the carbazolide 8-position and carbene sulfur; α, N2−Cu−C1 angle; β, dihedral angle between carbazolide and carbene planes; γ, dihedral angle between Dipp and carbene planes. The bottom row shows space-filling representations of the molecules. Carbazolides are highlighted in green, Dipp rings are shown in red, and the phenyl ring at the 1,3-thiazol-2-ylidene is presented in blue.

based emitters, featuring a flat molecular geometry and reduced steric encumbrance of the carbene moiety. A simultaneous electroluminescence from the bluish green emitting monomer and orange-red emitting excimer allowed the preparation of efficient single-emitter WOLEDs, following the concept widely applied in the case of square-planar-coordinated Pt(II) complexes.[36,37] A vacuum-deposited WOLED featuring emitter **7** achieved an external quantum efficiency (EQE) of 16.5%, a maximum brightness exceeding 40000 cd/m^2, and a color rendering index (CRI) of over 80. The presented results not only expand the structural diversity of coinage-metal-based carbene−metal−amide emitters by introducing a novel carbene building block but also demonstrate a novel application direction for this emitter class. Namely, the compounds can be applied to develop highly cost effective WOLEDs for lighting applications, offering expense reduction through cheaper emitters and a simplified device architecture.

RESULTS AND DISCUSSION

Synthesis. *N*-2,6-Diisopropylphenyl (Dipp)-substituted 1,3-thiazol-3-ium perchlorate carbene precursors, modified with 4,5-dialkyl or 4-phenyl 5-methyl substituents (**9**, **11**, and **13**) were synthesized following literature procedures.[38] The preparation of two-coordinate carbene−Cu(I)−chloride complexes (**10**, **12**, and **14**) was carried out by *in situ* generation of a free carbene in the presence of CuCl (Scheme 1). Amide ligands were introduced by reactions of the chloride complexes and various deprotonated carbazolides: carbazole (Cbz), 1,8-dimethylcarbazole (MeCbz), 3,6-di-*tert*-butylcarbazole (*t*BuCbz), and 3,6-di-*tert*-butyl-1,8-dimethylcarbazole (Me*t*BuCbz). The target complexes **1**−**6** were obtained as white crystalline powders, whereas **7** was a light green and **8** a yellow solid. The compounds, with the exception of **6**, show moderate to good solubility in various aprotic organic solvents such as toluene, chlorobenzene, dichloromethane, and THF. Complex **6** exhibits much lower solubility and is only sparingly soluble upon heating. In the crystalline form the compounds are stable and can be stored indefinitely in the air. The decomposition temperatures (thermogravimetric analysis, 5% weight loss) vary in the range of 275−300 °C (Figure S1). A slight increase in decomposition temperatures (by approximately 15 °C) was observed for 4-phenyl-substituted 1,3-thiazol-2-ylidene derivatives **5**−**8** in comparison to 4-alkyl-substituted compounds **1**−**4**. Due to their sufficient thermal stability the compounds can be processed with a vacuum deposition technique.

Compound Structures. Suitable single crystals for X-ray crystallographic analysis were successfully prepared for complexes **1**−**5** and **8** by layering solutions of THF with pentane.

https://doi.org/10.1021/acsami.2c00847
ACS Appl. Mater. Interfaces 2022, 14, 15478−15493

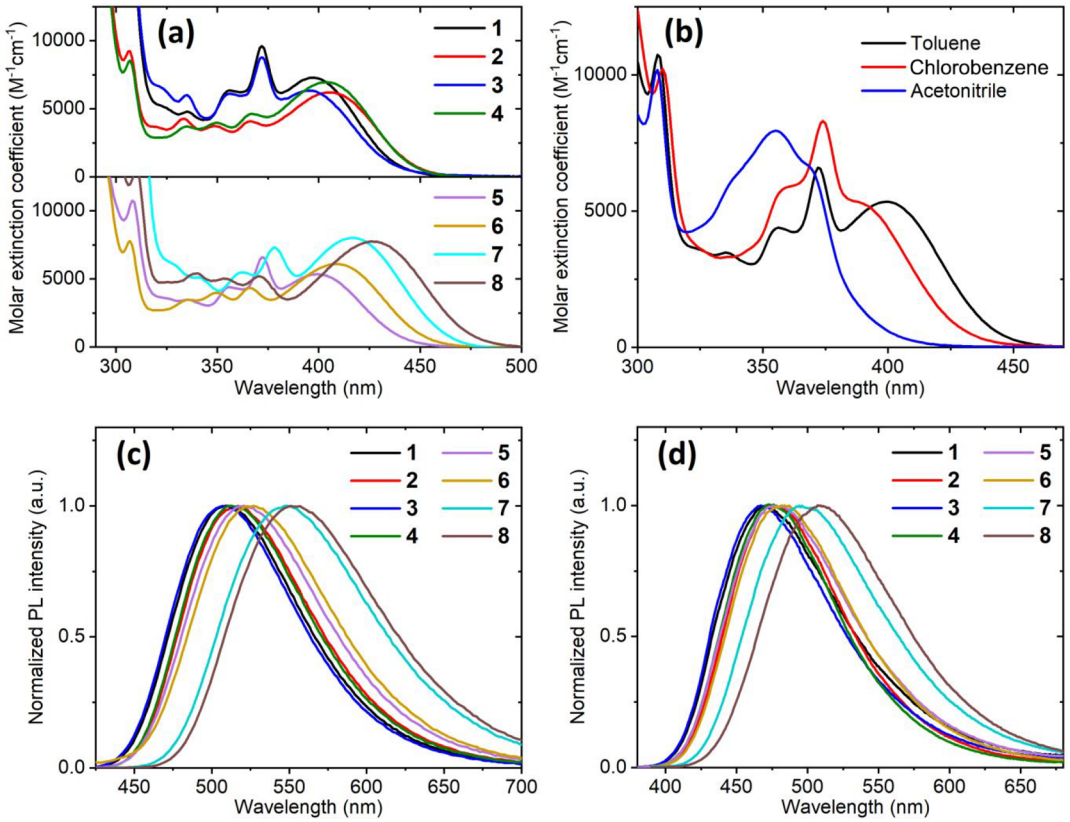

Figure 3. Photophysical properties of complexes **1**−**8**: (a) UV−vis absorption of complexes in toluene (10^{-5} M); (b) UV−vis absorption of **5** in toluene, chlorobenzene, and acetonitrile (10^{-5} M); (c) PL bands of complexes in deoxygenated toluene (10^{-5} M); (d) PL bands of complexes in doped PMMA films (5 wt %).

Crystal structures of the complexes and their key structural parameters are given in the Tables S1−S3 in the Supporting Information. While generally the complexes can be characterized with a near-linear geometry and an almost coplanar configuration between the carbazolide and carbene planes, the introduction of sterically demanding substituents at the 1,3-thiazol-2-ylidene (4-phenyl group) or at the carbazolide (1,8-dimethyl groups) causes various structural deformations (Figure 2). In the absence of steric strain the angle α (∠N2−Cu−C1) is slightly bent (~5°) in the direction of the Dipp ring (Figure 2a). If methyl groups are introduced at the 1,8-positions of the carbazolide, a repulsion takes place between the carbazolide methyl and the Dipp ring, twisting α in the direction of the unhindered side of the carbene ligand (Figure 2b). This steric interaction also causes a slight elongation of the metal−ligand bonds. The distances N2−Cu and Cu−C1 vary in the ranges of 1.845−1.855 and 1.859−1.871 Å, respectively, when Cbz is present, while for the complexes hosting MeCbz or Me*t*BuCbz ligands these values reach 1.866−1.871 and 1.873−1.887 Å, respectively. When a phenyl group is attached at the 4-position of the thiazol-2-ylidene, an additional structural deformation is introduced (Figure 2c). Due to a steric overcrowding at the carbene, phenyl and Dipp rings form a fan-shaped geometrical motif. As a result the Dipp ring is pushed out of the perpendicular alignment with the 1,3-thiazol-2-ylidene plane. Since the ring plane of the attached carbazolide is conformationally constrained to reside between the two isopropyl groups of Dipp, the rotation of the former structural fragment additionally moves the carbazolide outside of the coplanar alignment with the carbene ligand. Consequently, for structures **5** and **8**, the dihedral angle between carbazolide and carbene planes (β) reaches a value of about 15°. On consideration ot the previous points, the molecules in which both previously mentioned steric factors are present should possess a reduced conformational freedom in terms of the ability of the carbazolide, Dipp, and phenyl rings to rotate around the corresponding linking bonds. Due to steric pressure from both the carbene and carbazolide sides, the isopropyl groups of Dipp act as a conformational lock, as can be seen in the space-filling representation of molecule **8** (Figure 2c). We directly relate the low outlier solubility of complex **6** to the increased structural rigidity of the compound, as it enhances the compound's crystallization tendency. While a similar low solubility would be expected for **8**, it is presumably prevented by the *tert*-butyl groups at the carbazolide, which limit close contacts between the molecules upon solid-state packing. As will be discussed further, the introduction of the previously discussed steric factors have a direct influence on the photophysical properties of the compounds.

Electrochemistry. Cyclic voltammetry (CV) measurements for solutions in acetonitrile were carried out to gain insight into the electrochemical properties of the complexes (Figure S2 and Table S4). Redox potentials were calibrated against the potential of the Fc^+/Fc reference. The compounds exhibit similar electrochemical behavior with quasi-reversible oxidation and irreversible reduction waves. The measured reduction potentials (E_{red}) are almost identical (approximately −2.28 V) for the whole series and are assigned to the reduction of the thiazol-2-ylidene carbene ligand. The oxidation process, on the other hand, is related to the carbazolide fragment. A small cathodic

https://doi.org/10.1021/acsami.2c00847
ACS Appl. Mater. Interfaces 2022, 14, 15478−15493

Table 1. Emissive Properties of Complexes 1−8 in Different Media

compound	λ_{max}, nm	Φ_{PL}	τ, μs	k_r,[a] 10^5 s^{-1}	k_{nr},[b] 10^5 s^{-1}	τ, μs (77 K)
			Toluene Solution			
1	511	0.37	0.58	6.4	10.9	
2	517	0.42	0.75	5.6	7.7	
3	507	0.41	0.36	11.4	16.4	
4	513	0.79	0.85	9.3	2.5	
5	521	0.39	0.46	8.5	13.3	
6	527	0.23	0.41	5.6	18.8	
7	549	0.73	0.72	10.1	3.6	
8	554	0.76	0.76	10.0	3.2	
			PMMA Films (5 wt %)			
1	471	0.74	2.6	2.8	1.0	187 (CT), 2536 (^{3}LE)
2	478	0.82	1.9	4.3	0.9	91 (CT), 2429 (^{3}LE)
3	467	0.68	1.9	3.6	1.6	199 (CT), 2919 (^{3}LE)
4	474	0.84	2.1	4.0	0.8	98 (CT), 2791 (^{3}LE)
5	479	0.71	2.1	3.4	1.4	167 (CT), 2367 (^{3}LE)
6	484	0.78	1.6	4.9	1.4	90(CT), 3046 (^{3}LE)
7	499	0.73	1.6	4.6	1.7	157 (CT), 2417 (^{3}LE)
8	509	0.86	1.2	7.2	1.2	117 (CT)

[a] $k_r = \Phi_{PL}/\tau$. [b] $k_{nr} = (1 - \Phi_{PL})/\tau$.

shift of the oxidation potential (E_{ox}) was observed with the introduction of electron-donating methyl and *tert*-butyl substituents. As a result, the E_{ox} value of the amide-centered process varies from 0.06 V for the Cbz-hosting complex **5** to −0.14 V for the Me*t*BuCbz-bearing complex **8**. In such a way the carbazolide ligand plays the main role in tuning the band gap (ΔE) values of the complexes. ΔE values vary in the range from 2.37 V for complex **3** to 2.13 V for complex **8**.

Photophysical Properties. UV−vis absorption spectra of the investigated compounds in toluene solutions are shown in Figure 3a. The structured absorption bands between 300 and 380 nm are assigned to local transitions of the carbazolide ligand.[25] The lowest-energy region features a single broad and structureless band, which undergoes a hypsochromic shift with increasing solvent polarity (Figure 3b). The solvatochromic response indicates a charge transfer (CT) nature of the transition. The negative solvatochromism of the CT bands is a distinctive characteristic of CMA complexes and is related to an inversion of the molecular dipole direction upon photoexcitation.[20,27,31] Similarly to other known CMAs, the CT transition is intense, with molar extinction coefficients ranging in the interval (5.3−8.0) × 10^3 M^{-1} cm^{-1}. A direct correlation between CT absorption energies and electrochemically determined band gap values can be made (Figure S3). The absorption onset energy of **8** is red-shifted by 0.23 eV in comparison to **3**, which corresponds well with the decrease in the ΔE value (0.24 V). This provides further evidence for the proposed carbazolide−carbene interligand CT character of the lowest-energy absorption bands.

The results of photoluminescence (PL) measurements in toluene solutions and doped PMMA films (5 wt %) are shown in Table 1. In toluene the complexes exhibit bluish green to green emission (λ_{max} = 507−554 nm; Figure 3c). The broad and featureless profile of the PL bands indicates emission from CT excited states. The relative spectral placement of PL bands is consistent with the CV and UV−vis absorption measurements. A large variation in the measured Φ_{PL} values is evident, ranging from 0.23 to 0.76, and is related to substantial differences in the nonradiative decay rates (k_{nr}). A clear correlation with regard to the complex structure can be made, where the compounds bearing 1,8-dimethyl carbazolide ligands (**2**, **4**, and **8**) show considerably lower k_{nr} values in comparison to the structural analogues with the Cbz fragment (**1**, **3** ,and **5**). As recently demonstrated by Li et al.,[39] the rotation of the donor ligand in CMA complexes plays a significant role in the excited-state deactivation process and the limitation of this conformational motion can be applied to significantly increase the PL efficiency of the compounds. As was discussed previously, a steric interaction between Dipp and the methyl groups of carbazolide is evident in the obtained X-ray structures and a conformational constraint is expected to take place in the corresponding complex molecules, limiting the ability of the carbazolide plane to rotate around the Cu−N bond and thus substantially reducing k_{nr}. The only exception from the observed trend is compound **6**, which shows the highest k_{nr} value among the series, despite the presence of the MeCbz ligand. This is attributed to the poor solubility of the compound and the prevalence of an additional nonradiative relaxation pathway, related to an aggregate formation.

Upon doping in PMMA (5 wt % emitter concentration) the complexes experience a substantial PL efficiency increase (Φ_{PL} = 0.71−0.86). This can be related to a nonradiative decay rate decrease, which arises due to the suppression of conformational motions in the solid state. Additionally, PL bands exhibit a pronounced hypsochromic shift in comparison to solutions, an effect that can be attributed to a characteristic rigidochromism of the CMA complexes.[20] While a slight variation is observed between nonradiative rates, k_r values of the compounds differ substantially, in the range of (2.8−7.2) × 10^5 s^{-1}. Again, a clear correlation with the complex structure can be made, where compounds with 1,8-dimethyl-substituted carbazolide ligands show a k_r increase by a factor of 1.1−1.6 in comparison to the structural analogues bearing a Cbz fragment. Notably, the highest radiative rates are observed for compounds **6** and **8**, which, in addition to s sterically demanding carbazole, feature a second steric factor—a phenyl substituent at the carbene ligand. These observations indicate that the limitation of the torsional motion of the carbazolide fragment has a positive effect on an enhancement in the k_r values.

https://doi.org/10.1021/acsami.2c00847
ACS Appl. Mater. Interfaces 2022, 14, 15478−15493

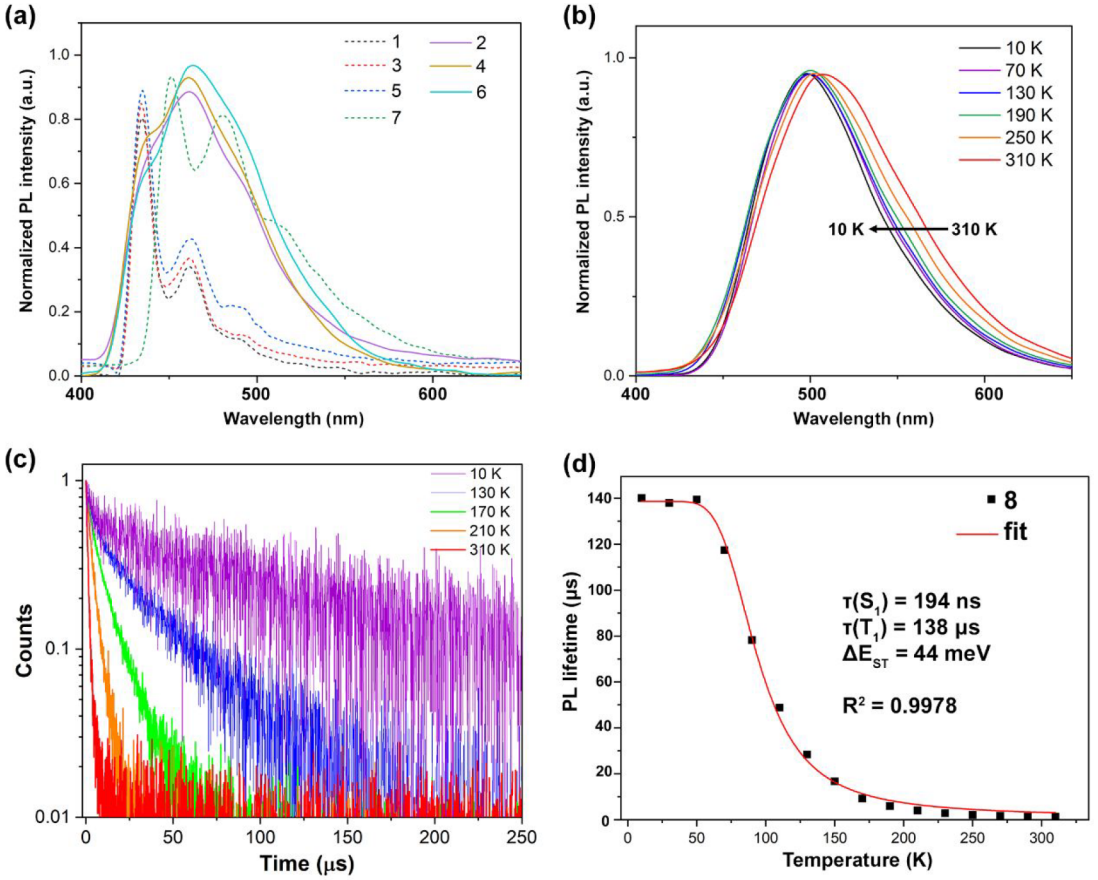

Figure 4. (a) PL bands of complexes **1**−**7** at 77 K in doped PMMA films (5 wt %). (b) PL bands of complex **8** at different temperatures. (c) PL decays of complex **8** at different temperatures. (d) PL lifetime and temperature correlation for complex **8** and fit against the Boltzmann relation. The parameters obtained from the fit, τ(S1), τ(T1), and ΔE_{ST} are provided.

In the examined PMMA films all of the compounds show monoexponential PL decay profiles (Figure S4). The lack of well-resolved prompt fluorescence and PL lifetimes in the range of a few microseconds indicates that the emission originates solely from the triplet states. This is a typical behavior for CMAs and is governed by large k_{ISC} values, which arise due to the significant SOC provided by the Cu atom.[21,40] Temperature-dependent measurements were performed for doped PMMA films to more deeply investigate the emissive mechanism of the compounds. PL spectra taken at 77 K (Figure 4a) indicate that for compounds **1**−**7** the emission bands transform, exhibiting a well-resolved vibrational substructure. The PL bands resemble the spectra of carbazole phosphorescence (Figure S5), demonstrating that the emission involves a relaxation from the local amide excited triplet (^{3}LE) states. The corresponding PL decays reveal a biexponential nature of the emission consisting of shorter (∼90−200 μs)- and longer-lived (∼2300−3000 μs) components (Figure S6). The CT and ^{3}LE nature of these two emissive processes is illustrated by time-resolved PL measurements (Figure S7). The prevalence of a ^{3}LE state emission under low-temperature conditions is characteristic among CMA emitters and is related to the destabilizing effect of the frozen host matrix, which shifts ^{1}CT and ^{3}CT levels above the ^{3}LE state, enabling the phosphorescence of the donor fragment.[20] A contrasting behavior is observed for compound **8**, which retains a structureless PL with CT character up to 10 K (Figure 3b). A blue shift of emission is evident, again illustrating the destabilizing effect on the CT state in response to the gradually solidifying host.

The PL kinetics of complex **8** was examined in the temperature interval 310−10 K (Figure 4c,d). The emission decays retain a monoexponential nature throughout the examined temperature range. A significant increase in PL lifetime is observed upon cooling, from 1.2 μs at room temperature to 140 μs at 10 K, illustrating a thermal activation of the emissive process and providing evidence for the TADF mechanism. Similarly to other TADF-active copper complexes three distinct temperature regions can be resolved.[14,41] At room temperature the emission originates predominantly from the ^{1}CT state, enabled by the TADF process. Upon cooling the ^{1}CT emission is progressively accompanied by a phosphorescence from ^{3}CT. Finally, below 50 K the emission lifetime no longer shows a temperature dependence, thus indicatint the sole contribution of ^{3}CT phosphorescence. A fit against the modified Boltzmann equation[41] was performed to obtain the ΔE_{ST} energy gap of the complex, yielding a value of 44 meV, which is comparable to the values observed in other high-performance CMA emitters.[21,35]

Theoretical Calculations. In order to gain a deeper insight into the mechanism of the emissive processes and establish the impact of steric effects on the emissive properties, a DFT analysis was performed. Compounds **5** and **6** were chosen for the calculations to account for structures with Cbz and bulky MeCbz amide ligands. Despite some small differences in S_1 and T_1 excited state energies for the two studied systems, the orbital

https://doi.org/10.1021/acsami.2c00847
ACS Appl. Mater. Interfaces 2022, 14, 15478−15493

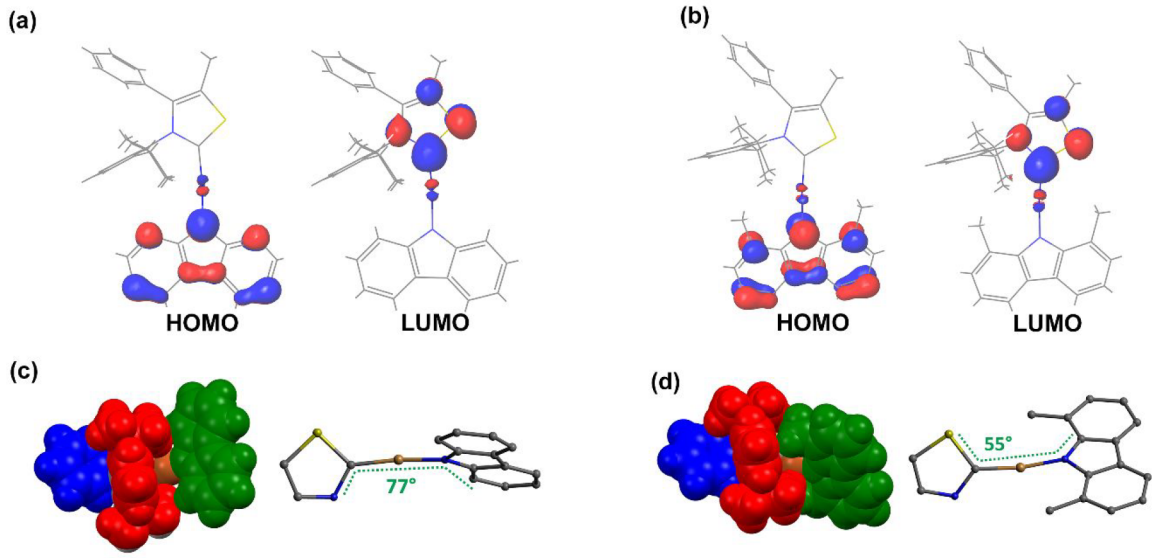

Figure 5. Frontier molecular orbitals of complexes **5** (a) and **6** (b) represented at the S_0 geometry of the compounds. Space-filling representations of the optimized S_1 state geometries and dihedral angles between the carbene and carbazolide planes for **5** (c) and **6** (d). Carbazolides are highlighted in green, Dipp rings are shown in red, and the phenyl ring at thiazol-2-ylidene is presented in blue.

Table 2. Selected Calculated Spectroscopic Parameters, Energetic Characteristics, and Rate Constants for Complexes 5 and 6

complex	ΔE_{ST}(ad), eV	λ_{abs}, nm ($f(S_0 \rightarrow S_1)$[a])	λ_{fl}, nm ($f(S_0 \rightarrow S_1)$[a])	λ_{phos},nm ($f(S_0 \rightarrow T_1)$[a])	$\langle S_1\lvert\hat{H}_{so}\rvert T_1\rangle$, cm^{-1}	λ(S),[b] eV	λ(T),[c] eV	k_p, s^{-1}	k_{fl}, s^{-1}	k_{ISC}, s^{-1}	k_{RISC}, s^{-1}
5	0.25	409 (0.115)	512 (0.011)	551 (3×10^{-5})[a]	42.5	0.07	0.19	2.2×10^3	2.7×10^6	8.9×10^{11}	1.2×10^6
6	0.23	418 (0.125)	538 (0.025)	568 (3×10^{-5})[a]	44.0	0.08	0.15	2.4×10^3	5.8×10^6	8.5×10^{11}	1.5×10^7

[a]The f value is given for the $S_0 \rightarrow T_1$ transition for the brightest triplet spin sublevel. [b]Reorganization energy associated with the RISC process. [c]Reorganization energy associated with the ISC process.

natures of these states are closely similar: the HOMO is localized on the carbazolide fragment, while the LUMO is situated on the carbene ring (Figure 5a,b). This allows us to assign the S_1 and T_1 states of complexes **5** and **6** to ligand to ligand charge-transfer (LLCT) excitations. The localization of HOMO and LUMO wave functions is found to be independent of the geometry (S_0, S_1, or T_1) at which they are computed. The HOMO and LUMO both contain some small contribution on the central Cu atom that affects the nonzero oscillator strength values for vertical $S_0 \rightarrow S_1$ absorption and $S_1 \rightarrow S_0$ emission, but that also leads to a considerably increased calculated adiabatic ΔE_{ST}(ad) gap (Table 2). In addition, our calculations reproduce well the small red shift in absorption and fluorescence maxima observed in experimental measurements of complex **6**.

In accordance with the X-ray structural data, the planes of the carbene and carbazolide ligand ring systems are practically coplanar at the optimized S_0 geometry. The same situation is observed for the T_1 state. However, at the S_1 geometry these planes tend to assume a perpendicular alignment (Figure 5c,d), as is commonly predicted among CMA emitters.[27,32,40] At the same time, the degrees of this structural transformation are not equal for the two complex molecules. While for compound **5** the dihedral angle between the carbene and carbazolide planes is 77°, in the case of **6** this value reaches only 55°. This can be directly attributed to the conformational locking effect, as during the rotation around the carbazolide−metal bond the methyls of the carbazolide in complex **6** cannot cross past the isopropyl groups of Dipp. Consequently, in the excited state the compound is bound to assume a semitwisted conformation. This has a profound effect on the predicted photophysical properties of the compound. While at the S_0 geometry the oscillator strengths (f) of the $S_0 \rightarrow S_1$ transition are almost identical for the two complexes, at the optimized S_1 state a 2-fold increase in f is observed for **6**, resulting in an equal increase in the predicted fluorescence rate (k_f). In CMA emitters the extent of electronic coupling between the two fragments involved in the LLCT process is directly dependent on the dihedral angle between them, where f is maximum at the coplanar configuration but practically zero at the perpendicular alignment.[40,42]

Combining the calculated values of adiabatic singlet−triplet splittings, reorganization energy values, and computed SOC matrix elements (SOCMEs) within the semiclassical Marcus theory expression,[43] we have estimated the rates of ISC (k_{ISC}) to be at the levels of 8.9×10^{11} and 8.5×10^{11} s^{-1} for complexes **5** and **6**, respectively. Using the calculated ΔE_{ST}(ad) gap, we predict the corresponding k_{RISC} values to be equal to 1.2×10^6 and 1.5×10^7 s^{-1}, respectively. The photophysical pattern of the delayed fluorescence phenomenon in the complexes can be characterized accordingly: the rate of ISC is much faster than the rate of prompt fluorescence k_p and thus prompt fluorescence is almost completely quenched by the ISC. Consequently, the rate-determining step of the emissive TADF relaxation pathway is the reverse intersystem crossing rate. When the experimental observations are taken into account, where the radiative rate of complex **6** is larger by a factor of 1.4 than for **5**, this difference can be attributed to a combination of increased oscillator strength and k_{RISC} parameters in the case of compound **6**. The phosphorescence of the studied complexes is predicted to be a

https://doi.org/10.1021/acsami.2c00847
ACS Appl. Mater. Interfaces 2022, 14, 15478−15493

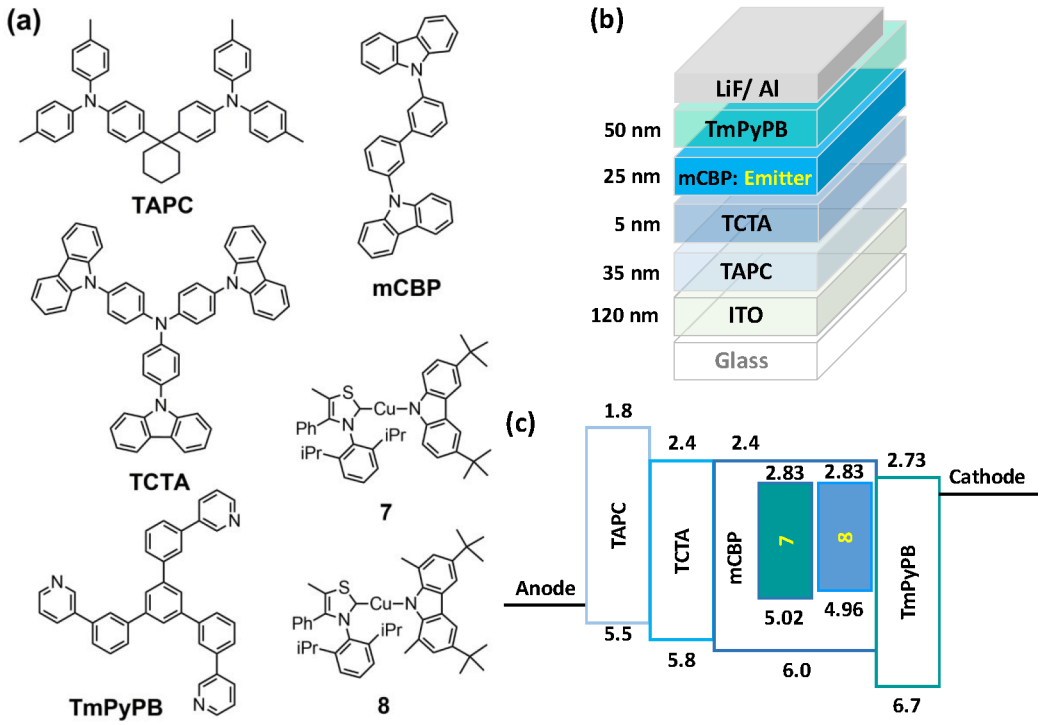

Figure 6. (a) Structural drawings of the materials used in the OLEDs. (b) Schematic structures of the fabricated OLEDs with different emitters. (c) Energy level diagram of the devices.

process that is too slow ($k_p \approx 2 \times 10^3$ s^{-1}) to compete with the fluorescence channel under room-temperature conditions. Only one individual sublevel of T_1 state demonstrates the ability to phosphorescence with a reasonable radiative lifetime (152 and 140 μs for **5** and **6**, respectively), while the two other spin sublevels are degenerate and demonstrate 2 orders of magnitude longer radiative lifetimes. The calculated values of ZFS between these dark spin sublevels and the upper bright spin substate are 2.9 and 5.7 cm^{-1} for **5** and **6**, respectively.

Electroluminescence Properties. To investigate the electroluminescent (EL) applications of thiazoline-based Cu(I) complexes **7** and **8**, we fabricated OLEDs to examine the carrier balance conditions using several potential hosts with adequate triplet energy gaps, including 4,4′-*N*,*N*′-dicarbazole-biphenyl (CBP),[44] 3,3′-bis(9*H*-carbazol-9-yl)-1,1′-biphenyl (mCBP),[45] 3-bis(9-carbazolyl)benzene (mCP),[46] and bis(2-(diphenylphosphino)phenyl)ether oxide (DPEPO).[47] Furthermore, the hole-transporting 1,1-bis[(di-4-tolylamino)phenyl]-cyclohexane (TAPC) and 4,4′,4″-tris(*N*-carbazolyl)-triphenylamine (TCTA) were combined to form a stepwise hole-transport layer (HTL), aiming to promote a smooth hole injection from the HTL into the emitting layer (EML).[48] On the other hand, 1,3,5-tris[(3-pyridyl)-phen-3-yl]benzene (TmPyPB) was used as the electron transport layer (ETL),[49] due to its excellent carrier transport capability of 1×10^{-3} cm^2/(V s) and a wide triplet energy gap (E_T) of 2.78 eV. The device with mCBP outperformed those with the other host materials. Furthermore, given the different inherent properties of the target compounds, we carefully regulated the thicknesses of each layer to optimize the EL efficiency. Consequently, two series of devices (i.e., compound **7** for device A and compound **8** for device B) were fabricated with the following generalized architecture: ITO/TAPC (35 nm)/TCTA (5 nm)/mCBP doped with a certain weight percent of compound **7** or **8** (25 nm)/TmPyPB (50 nm)/LiF (1.5 nm)/Al (150 nm), where the ITO and aluminum were respectively used as the anode and cathode. The doping concentrations used were set to 1, 5, 10, and 20 wt % to examine the influence of the emitter spatial distance and device carrier balance. The materials used, schematic architectures, and energy level diagrams of the fabricated OLEDs are given in Figure 6.

Figure 7 shows the EL characteristics of the device series A, featuring different doping concentrations. The corresponding numerical data collected from the figures are summarized in Table 3. As shown in Figure 7a, all tested devices regardless of emitter concentration display two distinct emission bands in the EL spectra. It is notable that the tested devices presented a similar behavior, that is, two-peak spectral profiles, with all screened host materials. The EL spectra of the tested devices with different host−guest systems are shown in Figure S8. As indicated, the emission peak at around 600 nm was akin to those using mCBP as a host. Accordingly, we can rule out the host material being responsible for the origin of the peak at around 590−600 nm. In addition, the slight red shift in the emission peak at around 495 nm with higher doping concentrations is likely due to solvation effects. With an increase in the doping concentration the relative intensity ratio between the emission peaks around 495 and 590 nm increased in the favor of the latter. Consequently, as the doping concentration is increased, the EL color changes from bluish green to warm white. The peak at around 495 nm was recognized as compound **7**'s TADF emission, while the 590 nm peak was preliminarily speculated to be an excimer emission originating from compound **7**'s dimer.[50,51] The observed emission with a broad spectral profile benefits the design of high-quality WOLEDs with high color rendering indices (CRI). With the EL spectrum of device A3 measured at a luminance of 1000 cd/m^2 as an example, the CRI and correlated color temperature (CCT) were respectively estimated to be 83.2 and 4240 K, demonstrating compound **7**'s potential for the construction of a high-quality lighting source.[52]

https://doi.org/10.1021/acsami.2c00847
ACS Appl. Mater. Interfaces 2022, 14, 15478−15493

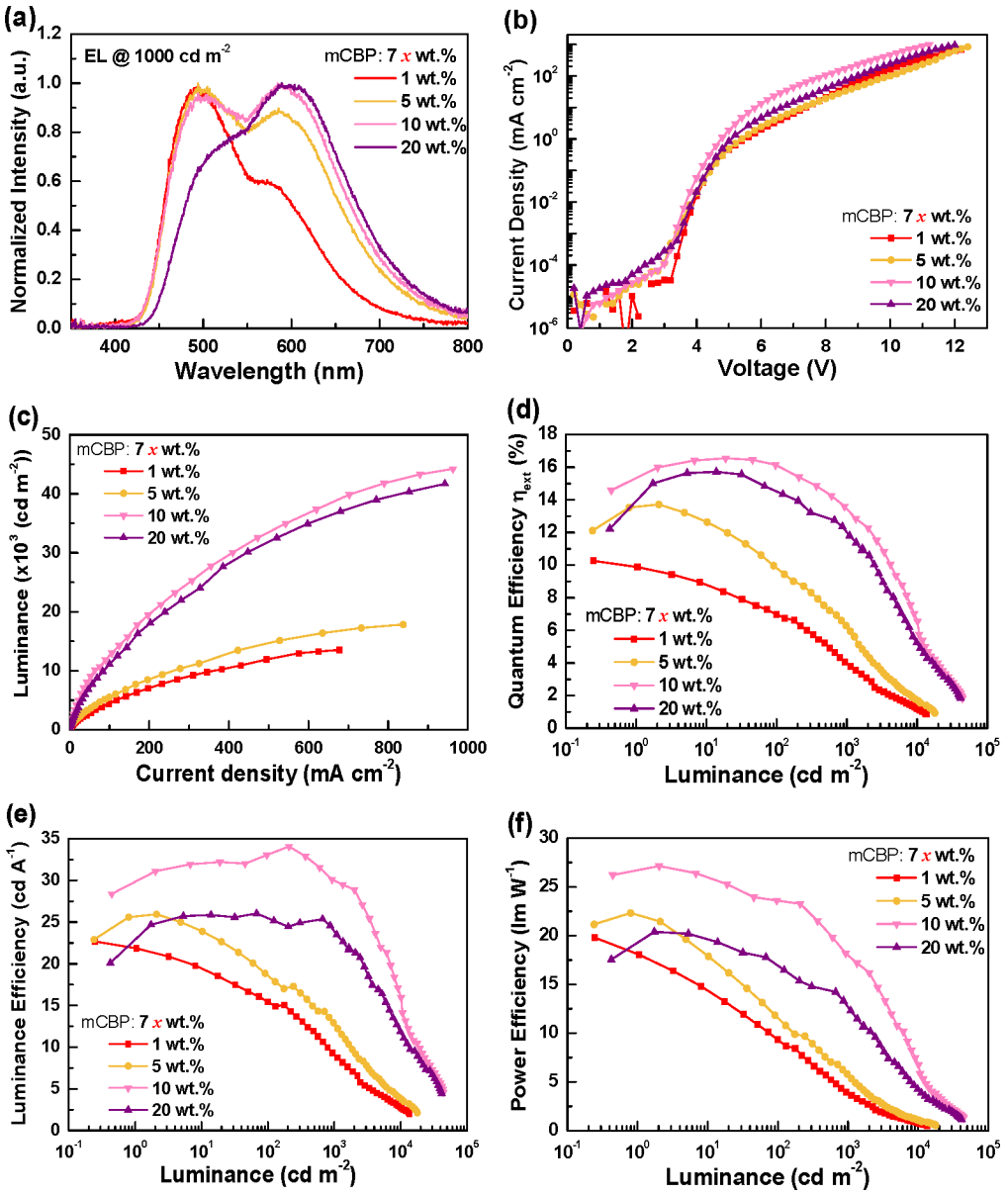

Figure 7. (a) Normalized EL spectra at a luminance of 10^3 cd m^{-2}, (b) current density−voltage (J−V) characteristics, (c) luminance−current density (L−J) characteristics, (d) external quantum efficiency vs luminance, (e) luminance efficiency vs luminance, and (f) power efficiency vs luminance for devices A1−A4.

The PL spectra of the doped films and the corresponding lifetime measurements were obtained and are discussed later, in order to clarify the origin of the emission.

Figure 7b,c respectively show the current density−voltage (J−V) curves and luminance−current density (L−J) curves. As indicated, device A3 (10 wt %) possesses the highest current density and luminance of all the devices. The higher current density suggests the adequate carrier transport capability of 7. The device's turn-on voltage (defined at a luminance of 1 cd/m^2) was also slightly decreased from 3.8 to 3.5 V as the doping concentration increased from 1 to 10 wt %. However, excessive doping concentrations might negatively affect the carrier transport characteristics of the EML. The EL spectrum of device A3 presents a dual emission consisting of a relatively weaker 7 emission and a stronger excimer emission. Therefore, the higher turn-on voltage might also be the result of the slightly inferior excimer efficiency. On the other hand, the EL spectra of all the devices presented emissions originating from compound 7, indicating that in all cases excitons formed in the EML and energy were effectively transferred from the host to the emitter. Hence, in comparison to the luminance at the same current density, we speculate that the higher luminance observed in device A3 might result from the relatively better carrier balance and the higher current density. When the doping concentrations exceeded 10 wt %, the carrier balance was gradually destroyed, leading to a reduction in device luminance. The maximum luminance of device A3 measured at 11.2 V reached 44215 cd/m^2, while that of device A4 with a higher doping concentration of 20 wt % was lowered to 41695 cd/m^2.

Similarly, the efficiency curves shown in Figures 7d−f indicate that device A3 outperformed the devices using other doping concentrations. The maximum external quantum efficiency (EQE) of device A3 reached 16.5%. Clearly, the peak efficiency of the tested devices rose with doping concentrations of 1−10 wt

https://doi.org/10.1021/acsami.2c00847
ACS Appl. Mater. Interfaces 2022, 14, 15478−15493

Table 3. EL Characteristics of Tested Devices with Different Emitters

	device							
	host/emitter							
	mCBP/7				mCBP/**8**			
	A1	A2	A3	A4	B1	B2	B3	B4
doping concentration (wt %)	1	5	10	20	1	5	10	20
external quantum efficiency (%)	10.3	13.7	16.5	15.7	12.9	12.2	9.2	5.9
a								
b	7.0	9.8	16.1	14.6	10.6	11.6	9.1	5.8
luminance efficiency (cd A^{-1})								
a	22.7	25.9	34.1	26.0	31.5	31.9	21.7	14.8
b	15.4	18.6	33.1	25.5	25.8	30.4	21.6	13.4
power efficiency (lm W^{-1})								
a	19.8	22.3	27.1	20.2	25.4	26.0	15.5	9.4
b	9.3	11.6	23.6	17.0	17.0	20.4	13.2	8.6
V_{on} (V)[c]	3.8	3.6	3.5	3.7	3.7	3.6	3.8	3.8
max luminance (cd m^{-2}) [V]	13542 [12.2]	17839 [12.4]	44215 [11.2]	41695 [12.0]	35947 [11.2]	42773 [11.2]	36478 [11.6]	37183 [12.4]
CIE1931 coordinates[b]	(0.30, 0.41)	(0.36, 0.42)	(0.38, 0.42)	(0.43,0.46)	(0.25,0.42)	(0.26,0.45)	(0.30, 0.45)	(0.36, 0.48)

[a]Maximum efficiency; [b]Measured at 10^2 cd m^{-2}. [c]Turn-on voltage measured at 1 cd m^{-2}.

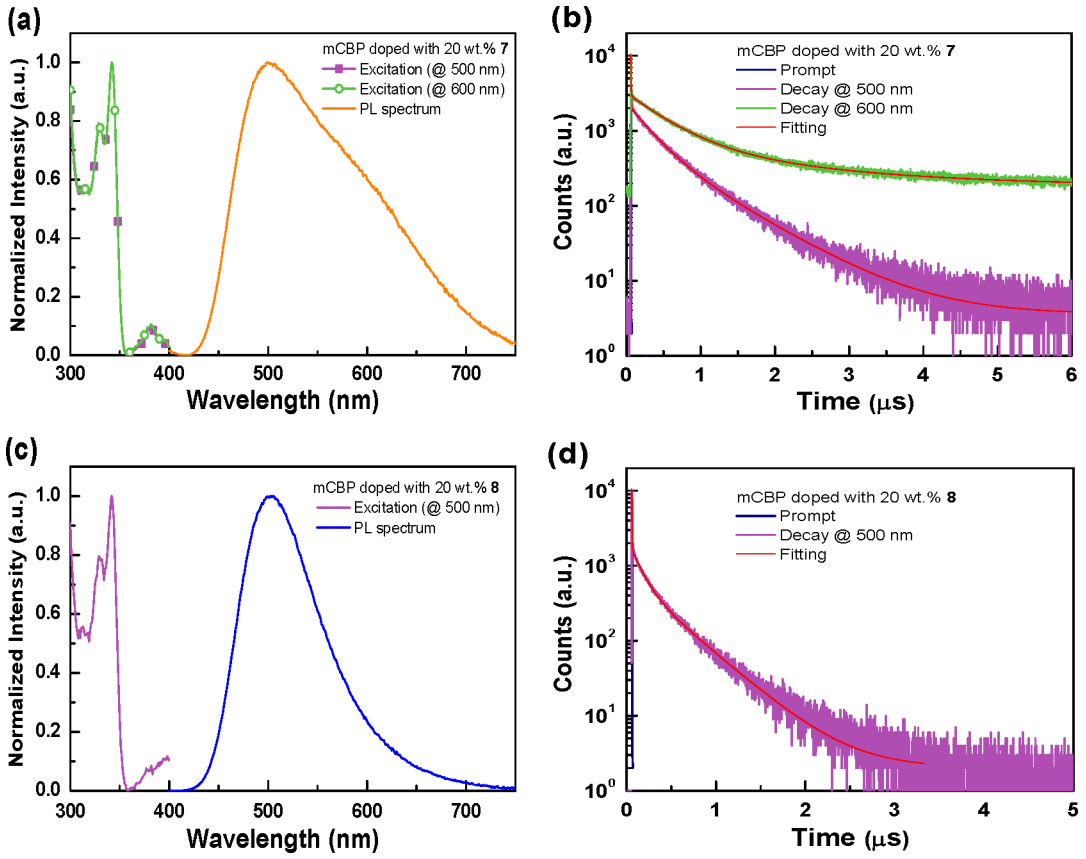

Figure 8. Photophysical properties of 20 wt % **7** doped in an mCBP host: (a) excitation and PL spectra; (b) the transient decay. Photophysical properties of 20 wt % **8** doped in an mCBP host: (c) excitation and PL spectra; (d) the transient decay.

% and then decreased when the doping was increased to 20 wt %, displaying an optimum range of the doping concentrations for compound **7**. At a higher practical luminance of 10^2 cd/m^2, the EQE values of devices A1−A4 presented efficiency drops of 30.8%, 28.5%, 2.4%, and 7.0% of their respective peak values in comparison to those recorded at 10^2 cd/m^2, respectively. The mitigated efficiency rolloff obtained in devices A3 and A4 might be attributed to the extended exciton formation zone with a stable carrier balance, thus mitigating triplet−triplet annihilation (TTA).[53] On closer investigation of the EL spectra (see Figure S9 in the Supporting Information), all tested devices revealed TADF and excimer dual emissions at low operating voltages. The excimer emission peak gradually weakened as the voltage increased. Notably, the high efficiency of device A3 was due to both the TADF and excimer, illustrating the adequate efficiency of the excimer.

The device architecture of series B (compound **8**) was the same as that of series A except for the emitter, as shown in Figure

https://doi.org/10.1021/acsami.2c00847
ACS Appl. Mater. Interfaces 2022, 14, 15478−15493

6. The EL characteristics and the corresponding numeric data of the series B devices are presented in Figure S10 and S11 and Table 3. Figure S10a shows the EL spectra of the devices with different doping concentrations of compound **8** recorded at 1000 cd/m^2. The lack of additional emission resulting from the host or carrier transport materials indicated an effective carrier recombination and excellent exciton confinement. A scenario similar to that for series A was observed for series B, where the excimer emission increased with the doping concentration. Nevertheless, the EL spectra revealed that the excimer emission was negligible when the doping concentrations were less than or equal to 5 wt %. In comparison to series A, the generalized excimer was considerably weaker in the series B devices, indicating that compound **8** with methyl groups at the 1,8-positions of carbazolide provides a steric repulsion to avoid molecular stacking.

Figure S10b shows the $J-V$ curves. As indicated, the tested devices exhibited similar current densities, indicating that the doping concentrations did not significantly affect the carrier transport. Nevertheless, the turn-on voltages of the series B devices gradually decreased to 3.6 V when the doping concentrations increased to 5 wt %. The turn-on voltages then increased to 3.8 V when doping concentrations exceeded 5 wt %, similar to the case for the series A devices. As shown in Figure S10c, devices B1, B3, and B4 possessed similar maximum luminances of around 36000−37000 cd/m^2 while a relatively higher value of 42773 cd/m^2 was obtained in device B2.

In contrast to the efficiency parameters observed in series A, the maximum efficiency was achieved in device B1 with the smallest doping amount of compound **8** (i.e., 1 wt %). With reference to Figures S10d−f, the optimized doping range of compound **8** is from 1 to 5 wt %. As indicated, the efficiencies of the series B devices were slightly inferior to those of series A. The respective peak efficiencies of devices B1−B4 reached 12.9%, 12.2%, 9.2%, and 5.9%. At a higher practical luminance of 10^2 cd/m^2, the devices B1−B4 represented efficiency drops of 17.8%, 4.9%, 1.1%, and 1.7% of their respective peak values in comparison to those recorded at 10^2 cd/m^2, respectively. In comparison to the series A devices, series B exhibited significantly mitigated efficiency rolloff, possibly due to the superior obstruction in space, inhibiting TTA. Overall, device doping concentrations with compounds **7** and **8** could be carefully adjusted to regulate the carrier balance and emission, tailoring the devices to meet specific application needs: single-color or white emission.

A comparison between the investigated CMA compounds and the previously reported top-performing structures in the terms of the device performance is outlined in Table S5.[19,20,23,25,26,28,33,54] While compound **7** does not show the highest EL efficiency, it is the only emitter that generates dual emission with tunable intensity via varying the doping concentration, realizing white-light emission with a single emitter. In addition, the maximum luminance of the white-emitting device with **7** can be as high as 44215 cd/m^2, indicating that the device has an excellent potential for lighting applications.

Excimer Characterization. To further corroborate the suspected excimer emission observed in the devices, two mCBP-hosted films with 20 wt % **7** or **8** content were fabricated by vacuum deposition to study the photodynamics in the solid state. Parts a and c of Figure 8 respectively show the excitation and photoluminescence (PL) spectra of films FA (compound **7**) and FB (compound **8**). The PL spectrum of film FA exhibits dual-emission peaks at around 500 and 600 nm, akin to the EL spectrum of device A4. Thus, we separately monitored the excitation spectra at 500 and 600 nm, aiming to distinguish the origins of the two peaks. Nevertheless, both excitation spectra are nearly identical, indicating the same structural origin of the two emissive processes. In other words, the newly formed peak at 600 nm retains the excitation profile of compound **7** and thus can be reasonably recognized as the excimer emission.[55] Parts b and d of Figure 8 respectively show the time-resolved photoluminescence (TRPL) measurements of films FA and FB. The TRPL measurement of film FA was also monitored at 500 and 600 nm. Interestingly, in comparison to measurements in diluted PMMA films, where the decay was predominantly monoexponential, the curves present a three-component decay, including a nanosecond-scale prompt term and two microsecond-scale delayed components. The fitting results are collected in Table S6. The prompt component of the lifetime (t_p) monitored at 500 nm was 2.74 ns, while the two delayed terms (t_d) were evaluated as 0.282 and 0.754 μs. For the 600 nm case, the respective t_p and t_d values were estimated to be 3.85 ns, 0.497 μs, and 1.875 μs. Although the measurements at 500 and 600 nm cannot strictly distinguish between monomer and excimer emissions, the significant difference in PL lifetimes affirm that the emission at each respective wavelength originates from a separate excited entity.[55] In contrast, the PL spectrum of film FB presents only a single peak (cf. Figure 8c), indicating a weaker excimer formation by photopumping. The lifetimes t_p and t_d of film FB monitored at 500 nm were respectively estimated to be 2.28 ns, 0.111 μs, and 0.424 μs. Clearly, the delayed terms (t_d) of **8** were shorter than those of **7**, which facilitates the fast relaxation of the excited state, thereby reducing the efficiency rolloff, as seen for the series B devices.

Only a few reports have attributed excimer formation to Cu(I)-based CMAs or closely related structures, where this phenomenon was observed in either doped films or solutions.[20,56] Practical EL from excimers, however, until now has not been reported among the class of Cu organometallic complexes. From a structural point of view, the more pronounced excimer formation tendency of thiazoline-based CMAs seems logical, as the lack of a bulky substituent at the sulfur atom differentiates this structure from its counterparts, which feature two isolating groups at each side of the carbene-forming carbon. In such way face to face close contacts are more likely to take place.

The relationship between the degree of steric encumbrance of the CMA emitter and its excimer formation tendency can be clearly seen among the investigated series of compounds. PL measurements of crystalline powders of complexes **1**−**4**, **7**, and **8** (samples **5** and **6** were not emissive) are given in Figure 9a. The PL band placement of the crystalline samples in almost all cases is close to that observed in solution or the diluted PMMA films (Figure 3c,d). The only exception is the benzene-grown crystal polymorph of complex **3**, which shows a substantial emission band red shift with a maximum at 570 nm. Subsequent PL measurements in highly concentrated (50 wt %) PMMA films (Figure 9b) relate this red-shifted band to the excimer emission, as the sample containing complex **3** exhibits two PL bands, a weaker band at approximately at 500 nm, attributed to monomer emission, and a stronger band at 560 nm, originating from an exciplex. As in the case of the previously examined mCBP-hosted samples, the PL lifetime of the red-shifted emission band (560 nm) is about 2-fold longer than that for the emission at 500 nm (Figure S12). In contrast, complex **4**, which features a

https://doi.org/10.1021/acsami.2c00847
ACS Appl. Mater. Interfaces 2022, 14, 15478−15493

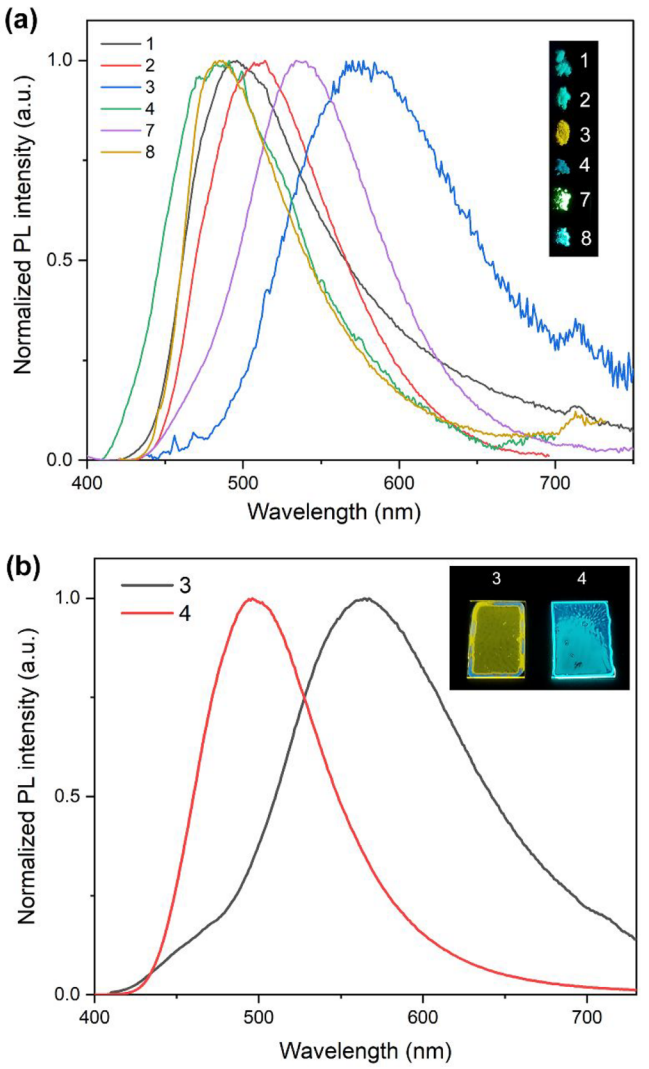

Figure 9. PL bands of crystalline powders of complexes **1**−**4**, **7**, and **8** (a). PL bands of PMMA doped (50 wt %) films containing emitters **3** and **4** (b). Insets show photographs of the corresponding UV (365 nm)-irradiated samples.

bulkier 1,8-dimethylcarbazole donor fragment, exhibits only monomer emission. Such a relation can be seen for the rest of the compound series (Figure S13), where the introduction of bulky substituents at the carbazolide leads to the disappearance of the excimer emission band (see PL bands **1** vs **2** and **5** vs **6**). This clearly illustrates that the steric shielding of the complex surface obstructs the formation of emissive dimers. In such a context it is not surprising that the most pronounced excimer formation is observed for complex **3**, which, in addition to the unsubstituted carbazole donor, is composed of a 1,3-thiazoline acceptor with the smallest methyl substituents.

Neither crystals nor concentrated PMMA films of compounds **7** and **8** show notable signs of excimer emission. This can be explained by the more pronounced steric shielding of the molecules, due to the presence of the massive *tert*-butyl groups at the carbazole moiety. In contrast to the previously discussed vacuum-deposited samples, no excimer formation was evident in solution-processed mCBP films of **7** (20 wt %) (Figure S14). On this basis, we speculate that the excimer formation for **7** and **8** is aided by vacuum deposition, which may facilitate specific packing patterns and enable formation of emissive dimers despite the presence of the bulkier substituents. The tendency of formation of alternatively emissive polymorphs among the investigated emitter class is demonstrated in the case of complex **3**, for which THF/pentane-grown crystals show a PL band with a maximum at 500 nm, characteristic of monomer emission (Figure S15), in contrast to the previously discussed excimer-forming polymorph obtained from benzene (Figure 9a).

The planar geometry and reduced steric encumbrance relate the structures of the studied thiazoline CMA emitters to square-planar-coordinated Pt(II) complexes, a compound class that is well-known for its excimer formation ability.[57] Such a property of Pt(II) emitters is frequently exploited to construct excimer-based single-emitter WOLEDs.[36,37,58−60] It is evident that the performance level of our presented device A3 is comparable to that of the aforementioned examples. In addition to the use of much cheaper Cu metal atoms, thiazaoline-based CMA emitters provide a potential benefit in the form of improved device CRI, as EL originates from wide overlapping emission bands of the monomer and excimer, whereas monomer emission in the case of Pt(II) complexes often has a narrower and structured emission band profile.

CONCLUSIONS

We have demonstrated that 1,3-thiazoline carbenes can be successfully used as building blocks for efficient CMAs, yielding emitters with Φ_{PL} values of up to 0.86. With the structural modification of the attached carbazolide the emission color of the compounds can be varied from bluish green to green. Similarly to other known CMA emitters the emissive mechanism is attributed to the TADF process. The radiative rates of the compounds are relatively high and vary in the range of $(2.8-7.2) \times 10^5\ s^{-1}$. X-ray structural analysis and DFT modeling relate the k_r increase among the investigated structural derivatives to the conformational locking of the carbazolide, which increases the coplanarity between the constituting fragments involved in the charge transfer process. This effect can be induced by a simultaneous attachment of bulky substituents at the carbene and carbazolide ring systems. The compounds possess a sufficient chemical stability for vacuum deposition and subsequent OLED integration. Together with the known structures featuring CAAC or MAC carbenes, this makes 1,3-thiazoline-based emitters the third example of copper-containing CMAs with a demonstrated OLED use.

For the first time among the compound class of organometallic copper complexes we have observed an efficient excimer electroluminescence. From a structural point of view this can be attributed to the reduced steric encumbrance of the 1,3-thiazoline-based complex surface, which allows closer solid-state molecular packing in comparison to the previously investigated CMA designs. At an optimal emitter concentration the devices based on emitter **7** showed a dual emission from monomers and excimers, producing single-emitter white color emission, with an EQE value of up to 16.5%. With the attained performance level being comparable to that of Pt(II) complex-based single-emitter WOLEDs, these results illustrate the prospects of copper-based materials as highly cost effective emitters for lighting devices.

EXPERIMENTAL SECTION

Synthesis and Characterization. All procedures involving the synthesis and purification of N-heterocyclic carbenes (NHC) derivatives were carried out under an inert atmosphere using Schlenk techniques. Unless specified otherwise, the materials and solvents used were purchased from commercial suppliers. Solvents (hexane, pentane,

https://doi.org/10.1021/acsami.2c00847
ACS Appl. Mater. Interfaces 2022, 14, 15478−15493

chlorobenzene, benzene, toluene, and acetonitrile) were distilled over CaH_2 and stored over molecular sieves (4 Å). Dry, air-free THF was distilled over K/benzophenone under N_2 prior to use. $CDCl_3$ was distilled over K_2CO_3 and stored over molecular sieves (4 Å). The starting compounds **9**, **11**, and **13**[38] and 1,8-dimethylcarbazole[61] were prepared by following the procedures described in the literature. NMR spectra were obtained on a Bruker Avance 300 MHz spectrometer using solvent residual signals as an internal reference ($CDCl_3$, ^1H δ 7.26 and ^{13}C δ 77.16; C_6D_6, ^1H δ 7.16 and ^{13}C δ 128.06). Elemental analysis was performed using a Costech Instruments ECS 4010 CHNS-O Elemental Combustion System. Decomposition temperatures were obtained using a PerkinElmer STA 6000 thermal analyzer.

General Method for Synthesis of Complexes 1−8. The synthesis and purification of complexes **1**−**5**, **7**, and **8** was carried out using dry, deoxygenated solvents (THF, hexane, and benzene). The carbazole (1,8-dimethylcarbazole, 3,6-di-*tert*-butylcarbazole, or 3,6-di-*tert*-butyl-1,8-dimethylcarbazole) and KOtBu were dissolved in THF and stirred for 30 min under an argon atmosphere. Then a THF solution of NHC-Cu-Cl was added dropwise via a syringe to the solution of the carbazole amide. The resulting mixture was stirred for 3 h at room temperature under an argon atmosphere and then filtered through a pad of Celite into hexane (approximately 200 mL) to precipitate the product. The resulting mixture was filtered to afford the product as a solid. Complexes **1**−**5** were recrystallized from benzene.

Compound ***1***. A solution of carbazole (0.161 g, 0.96 mmol) and KOtBu (0.108 g, 0.96 mmol) in THF (5 mL) and a solution of **10** (0.350 g, 0.88 mmol) in THF (13 mL) were used. Yield: 0.25 g (54%), white solid (after recrystallization from benzene). Crystals suitable for X-ray diffraction analysis were obtained by layering a solution of THF with pentane. ^1H NMR δ(H) ($CDCl_3$, 300 MHz): 8.00 (d, J = 7.6 Hz, 2H), 7.66 (t, J = 7.8 Hz, 1H), 7.43 (d, J = 7.8 Hz, 2H), 7.14 (t, J = 7.5 Hz, 2H), 7.01−6.86 (m, 4H), 2.92−2.83 (m, 2H), 2.32−2.20 (m, 4H), 1.96−1.80 (m, 4H), 1.28−1.17 (m, 12H). ^{13}C NMR δ(C) ($CDCl_3$, 75.47 MHz): 202.74, 150.12, 145.24, 143.91, 136.95, 133.10, 130.93, 125.07, 124.36, 123.39, 119.56, 115.39, 114.57, 28.75, 25.37, 24.32, 23.87, 23.37, 22.23, 21.71. Anal. Calcd for $C_{31}H_{33}CuN_2S$: C, 70.36; H, 6.29; Cu, 12.01; N, 5.29; S, 6.06. Found: C, 70.49; H, 6.36; N, 5.36.

Compound ***2***. A solution of 1,8-dimethylcarbazole (0.120 g, 0.61 mmol) and KOtBu (0.069 g, 0.61 mmol) in THF (3 mL) and a solution of **10** (0.222 g, 0.56 mmol) in THF (8 mL) were used. Yield: 0.21 g (68%), white solid (after recrystallization from benzene). Crystals suitable for X-ray diffraction analysis were obtained by layering a solution of THF with pentane. ^1H NMR δ(H) ($CDCl_3$, 300 MHz): 7.95 (d, J = 7.5 Hz, 2H), 7.60 (t, J = 7.8 Hz, 1H), 7.38 (d, J = 7.8 Hz, 2H), 7.10−7.03 (m, 2H), 6.96 (t, J = 7.3 Hz, 2H), 2.90−2.82 (m, 2H), 2.58 (s, 6H), 2.36−2.21 (m, 4H), 1.95−1.79 (m, 4H), 1.28−1.14 (m, 12H). ^{13}C NMR δ(C) ($CDCl_3$, 75.47 MHz): 148.92, 144.72, 144.25, 136.87, 133.05, 130.98, 125.17, 124.88, 124.48, 122.01, 117.55, 115.60, 28.69, 25.26, 24.60, 23.84, 23.58, 22.28, 21.76, 21.15. Anal. Calcd for $C_{33}H_{37}CuN_2S$: C, 71.12; H, 6.69; Cu, 11.40; N, 5.03; S, 5.75. Found: C, 71.19; H, 6.79; N, 5.07.

Compound ***3***. A solution of carbazole (0.172 g, 1.03 mmol) and KOtBu (0.116 g, 1.03 mmol) in THF (5 mL) and a solution of **12** (0.350 g, 0.94 mmol) in THF (20 mL) were used Yield: 0.14 g (30%), white solid (after recrystallization from benzene). Crystals suitable for X-ray diffraction analysis were obtained by layering a solution of THF with pentane. ^1H NMR δ(H) ($CDCl_3$, 300 MHz): 8.03 (d, J = 7.6 Hz, 2H), 7.69 (t, J = 7.7 Hz, 1H), 7.46 (d, J = 7.8 Hz, 2H), 7.17 (t, J = 7.5 Hz, 2H), 7.02−6.89 (m, 4H), 2.42 (s, 3H), 2.27 (hept, J = 6.8 Hz, 2H), 2.04 (s, 3H), 1.31−1.17 (m, 12H). ^{13}C NMR δ(C) ($CDCl_3$, 75.47 MHz): 202.58, 150.12, 145.18, 141.41, 138.06, 130.96, 130.67, 125.15, 124.35, 123.38, 119.55, 115.39, 114.58, 28.72, 25.35, 23.37, 12.62, 12.25. Anal. Calcd for $C_{29}H_{31}CuN_2S$: C, 69.22; H, 6.21; Cu, 12.63; N, 5.57; S, 6.37. Found: C, 69.47; H, 6.17; N, 5.74.

Compound ***4***. A solution of 1,8-dimethylcarbazole (0.202 g, 1.03 mmol) and KOtBu (0.116 g, 1.03 mmol) in THF (5 mL) and a solution of **12** (0.350 g, 0.94 mmol) in THF (20 mL) were used. Yield: 0.20 g (40%), white solid (after recrystallization from benzene). Crystals suitable for X-ray diffraction analysis were obtained by layering a solution of THF with pentane. ^1H NMR δ(H) ($CDCl_3$, 300 MHz): 7.96 (d, J = 7.6 Hz, 2H), 7.61 (t, J = 7.8 Hz, 1H), 7.39 (d, J = 7.8 Hz, 2H), 7.12−7.05 (m, 2H), 7.01−6.93 (m, 2H), 2.57 (s, 6H), 2.45 (s, 3H), 2.28 (hept, J = 6.5 Hz, 2H), 2.02 (s, 3H), 1.27−1.17 (m, 12H). ^{13}C NMR δ(C) ($CDCl_3$, 75.47 MHz): 148.91, 144.66, 141.72, 137.94, 131.01, 130.58, 125.23, 124.86, 124.48, 122.01, 117.54, 115.59, 28.66, 25.23, 23.55, 21.13, 12.61, 12.54. Anal. Calcd for $C_{31}H_{35}CuN_2S$: C, 70.09; H, 6.64; Cu, 11.96; N, 5.27; S, 6.04. Found: C, 70.16; H, 6.68; N, 5.31.

Compound ***5***. A solution of carbazole (0.148 g, 0.88 mmol) and KOtBu (0.099 g, 0.88 mmol) in THF (5 mL) and a solution of **14** (0.350 g, 0.81 mmol) in THF (15 mL) were used. Yield: 0.26 g (57%), white solid (after recrystallization from benzene). Crystals suitable for X-ray diffraction analysis were obtained by layering a solution of THF with pentane. ^1H NMR δ(H) ($CDCl_3$, 300 MHz): 8.02 (d, J = 7.6 Hz, 2H), 7.54 (t, J = 7.8 Hz, 1H), 7.41−7.23 (m, 5H), 7.21−7.05 (m, 4H), 7.03−6.89 (m, 4H), 2.50−2.36 (m, 5H), 1.33 (d, J = 6.7 Hz, 6H), 1.10 (d, J = 6.8 Hz, 6H). ^{13}C NMR δ(C) ($CDCl_3$, 75.47 MHz): 203.53, 150.09, 146.31, 145.25, 138.34, 133.26, 130.78, 130.26, 129.90, 128.66, 128.04, 124.69, 124.37, 123.39, 119.57, 115.40, 114.59, 28.98, 26.37, 22.63, 13.23. Anal. Calcd for $C_{34}H_{33}CuN_2S$: C, 72.24; H, 5.88; Cu, 11.24; N, 4.96; S, 5.67. Found: C, 72.24; H, 6.04; N, 5.04.

Compound ***6***. 1,8-Dimethylcarbazole (0.248 g, 1.27 mmol) and KOtBu (0.142 g, 1.27 mmol) were dissolved in a dry THF (15 mL) and stirred for 30 min under an argon atmosphere. Then a THF (40 mL) solution of **14** (0.50 g, 1.15 mmol) was added dropwise via syringe to a solution of carbazole amide. After approximately 5 min precipitation of the product was observed. The resulting mixture was stirred for 3 h at room temperature under an argon atmosphere and then filtered to offer the crude product as a solid. The crude product was purified by recrystallization from chlorobenzene and washed with dry THF. Yield: 0.35 g (51%), white solid. ^1H NMR δ(H) ($CDCl_3$, 300 MHz): 7.94 (d, J = 7.6 Hz, 2H), 7.47 (t, J = 8.0 Hz, 1H), 7.36−7.30 (m, 3H), 7.24−7.18 (m, 2H), 7.14−7.02 (m, 4H), 6.95 (t, J = 7.4 Hz, 2H), 2.65−2.53 (m, 6H), 2.50−2.37 (m, 5H), 1.29 (d, J = 6.7 Hz, 6H), 1.05 (d, J = 6.8 Hz, 6H). ^{13}C NMR data were not obtained due to the low solubility of the product in $CDCl_3$. Anal. Calcd for $C_{36}H_{37}CuN_2S$: C, 72.88; H, 6.29; Cu, 10.71; N, 4.72; S, 5.40. Found: C, 72.34; H, 6.47; N, 4.56.

Compound ***7***. A solution of 3,6-di-*tert*-butylcarbazole (0.281 g, 1.01 mmol) and KOtBu (0.113 g, 1.01 mmol) in THF (15 mL) and a solution of **14** (0.400 g, 0.92 mmol) in THF (20 mL) were used Yield: 0.30 g (48%), greenish yellow solid. ^1H NMR δ(H) (C_6D_6, 300 MHz): 8.47 (s, 2H), 7.59 (d, J = 8.0 Hz, 2H), 7.30−7.23 (m, 2H), 6.93 (d, J = 7.6 Hz, 2H), 6.86−6.67 (m, 6H), 2.34 (hept, J = 6.5 Hz, 2H), 1.57 (s, 18H), 1.42−1.32 (m, 9H), 0.86 (d, J = 6.3 Hz, 3H). ^{13}C NMR δ(C) (C_6D_6, 75.47 MHz): 203.70, 149.70, 145.81, 145.40, 138.60, 138.09, 133.60, 130.92, 130.31, 129.59, 125.55, 124.85, 121.61, 116.20, 114.55, 34.81, 32.73, 29.11, 26.32, 22.55, 12.04. Anal. Calcd for $C_{42}H_{49}CuN_2S$: C, 74.46; H, 7.29; Cu, 9.38; N, 4.14; S, 4.73. Found: C, 74.06; H, 7.22; N, 4.15.

Compound ***8***. A solution of 3,6-di-*tert*-butyl-1,8-dimethylcarbazole (0.309 g, 1.00 mmol) and KOtBu (0.113 g, 1.01 mmol) in THF (15 mL) and a solution of **14** (0.400 g, 0.92 mmol) in THF (20 mL) were used Yield: 0.50 g (77%), yellow solid. Crystals suitable for X-ray diffraction analysis were obtained by layering a solution of THF with pentane. ^1H NMR δ(H) (C_6D_6, 300 MHz): 8.44 (s, 2H), 7.54 (s, 2H), 7.06 (t, J = 7.8 Hz, 1H), 6.85−6.77 (m, 5H), 6.72−6.66 (m, 2H), 2.85 (s, 6H), 2.28 (hept, J = 6.8 Hz, 2H), 1.65−1.54 (m, 21H), 1.22 (d, J = 6.7 Hz, 6H), 0.78 (d, 6.8 Hz, 6H). ^{13}C NMR δ(C) (C_6D_6, 75.47 MHz): 205.50, 148.61, 146.20, 144.80, 138.47, 138.28, 133.18, 131.00, 130.31, 129.59, 126.11, 124.97, 123.16, 121.07, 114.29, 34.73, 32.75, 29.06, 26.20, 22.79, 22.08, 12.32. Anal. Calcd for $C_{44}H_{53}CuN_2S$: C, 74.91; H, 7.57; Cu, 9.01; N, 3.97; S, 4.54. Found: C, 74.87; H, 7.58; N, 4.14.

X-ray Crystallography. Single crystals of **1**−**5** and **8** ware obtained by layering the corresponding THF solutions with pentane. Crystallographic diffraction data were collected with a Rigaku XtaLAB Synergy, Dualflex, HyPix diffractometer (Cu Kα, λ = 1.54184 Å) equipped with a low-temperature Oxford Cryosystems Cryostream Plus device. The crystal structures were solved by direct methods with the ShelXT[62] structure solution program using an intrinsic phasing solution method. The crystal structures of **1** and **3** were refined with the SHELXL[63]

https://doi.org/10.1021/acsami.2c00847
ACS Appl. Mater. Interfaces 2022, 14, 15478−15493

refinement package using least-squares minimization. All of the other crystal structures were refined with a version of the program olex2.refine[64] using Levenberg–Marquardt minimization (for the structure of **2** using Gauss–Newton minimization). All calculations were performed with Olex2 software.[65] Table S1 gives the main crystal data for these compounds. Crystallographic data for **1**–**5** and **8** are deposited at the Cambridge Crystallographic Data Centre as the corresponding supplementary publications CCDC 2114050, 2114049, 2114046, 2114047, 2114048, and 2114045. Copies of the data can be obtained, free of charge, on application to the CCDC, 12 Union Road, Cambridge CB2 1EZ, U.K.

Cyclic Voltammetry Measurements. Cyclic voltammetry measurements were performed with a PARSTAT 2273 potentiostat. Electrochemical redox reactions were performed in anhydrous acetonitrile solutions under an Ar atmosphere using 0.1 M tetrabutylammonium hexafluorophosphate ($TBAPF_6$) as the supporting electrolyte. The measurements were carried out using a three-electrode cell configuration. A stationary glassy-carbon disk (Ø 0.5 cm) was used as the working electrode, Pt wire as the auxiliary electrode, and silver wire as the pseudoreference electrode.

Photophysical Measurements. UV–vis absorption and PL measurements in solution were carried with a material concentration of 1×10^{-5} mol L^{-1}. Solutions for Φ_{PL} and emission decay measurements were prepared in a glovebox under an Ar atmosphere using moisture-free and previously degassed solvents. PMMA films for optical measurements were prepared from chlorobenzene solutions (30 mg/mL material concentration) using a drop-casting method. After the deposition of the solution on glass slides the samples were immediately placed in a preheated oven and dried for 2 h at 80 °C. The UV–vis spectra were recorded with a PerkinElmer Lambda 35 spectrometer. Depending on the nature of the experiment, photoluminescence properties were measured on two different spectroscopic systems. Emission spectra, Φ_{PL}, and PL lifetimes for solution and thin films at room temperature, as well as PL spectra, time-resolved measurements, and PL lifetimes at 77 K (in a liquid-nitrogen-filled quartz Dewar), were measured with a QuantaMaster 40 spectrofluorometer (Photon Technology International, Inc.). Room-temperature PL measurements for doped films were carried out under an N_2 atmosphere. A 375 nm laser with a 60 ps pulse width and tunable repetition rate (between 1 mHz and 50 kHz) was used for the fast (nanosecond–microsecond range) kinetics measurements. A steady-state and pulsed (3 μs pulse width) xenon lamp was used for steady-state and millisecond kinetics measurements. The excitation source for temperature-dependent (10–300 K) photoluminescence measurements in a helium cryostat was a tunable Ekspla NT 342/3UV laser with a repetition rate of 10 Hz and 5 ns pulse width. Photoluminescence spectra and PL decays were obtained with a PMT apparatus attached to an Andor monochromator.

To acquire ΔE_{ST} values, PL lifetimes of compound **8**, measured in the temperature interval 310–10 K, were fitted against a modified Boltzmann equation[41]

$$\tau = \frac{1 + \exp\left(-\frac{\Delta E(S_1-T_1)}{k_B T}\right)}{\frac{1}{\tau_{T_1}} + \frac{1}{\tau_{S_1}}\exp\left(-\frac{\Delta E(S_1-T_1)}{k_B T}\right)} \quad (1)$$

where k_B is the Boltzmann constant, τ_{T_1} is the decay time of the emitting triplet state, τ_{S_1}, is the decay time of the emitting singlet state, and $\Delta E(S_1-T_1)$ is the energy gap between the S_1 and T_1 states.

OLED Preparation and Characterization. Organic materials purchased from Shine Materials Technology were subjected to temperature-gradient sublimation under high vacuum before use. After a routine cleaning procedure of ultrasonication of the ITO-coated glass in deionized water and organic solvents, the ITO substrate was pretreated with plasma for 5 min. The organic and metal layers were deposited by thermal evaporation in a vacuum chamber with a base pressure of $<10^{-6}$ Torr. Device fabrication was completed in a single cycle without breaking the vacuum. The deposition rates of organic materials and aluminum were respectively kept at around 0.1 and 0.5 nm s^{-1}. The active area was defined by a shadow mask (2×2 mm^2). Current density–voltage–luminance characterization was done using two Keysight B2901A current source-measure units equipped with a calibrated Si photodiode. The electroluminescent spectra of the devices were recorded using an Ocean Optics spectrometer (Ocean Optics 2000).

■ ASSOCIATED CONTENT

Supporting Information

The Supporting Information is available free of charge at https://pubs.acs.org/doi/10.1021/acsami.2c00847.

Synthetic procedures for intermediate compounds **10**, **12**, **14**, and 3,6-di-*tert*-butyl-1,8-dimethylcarbazole, description of procedures for theoretical calculations, thermogravimetry and single-crystal X-ray diffraction data, results of electrochemical and photophysical measurements, OLED characterization, NMR spectra, and coordinates for DFT-optimized structures (PDF)

Crystallographic information for complexes **1**–**5** and **8** (CIF)

■ AUTHOR INFORMATION

Corresponding Authors

Chih-Hao Chang – *Department of Electrical Engineering, Yuan Ze University, Chungli 32003, Taiwan;* orcid.org/0000-0002-5586-9526; Email: chc@saturn.yzu.edu.tw

Kaspars Traskovskis – *Faculty of Materials Science and Applied Chemistry, Riga Technical University, LV-1048 Riga, Latvia;* orcid.org/0000-0003-1416-7533; Email: kaspars.traskovskis@rtu.lv

Authors

Armands Ruduss – *Faculty of Materials Science and Applied Chemistry, Riga Technical University, LV-1048 Riga, Latvia*

Baiba Turovska – *Latvian Institute of Organic Synthesis, Riga LV-1006, Latvia*

Sergey Belyakov – *Latvian Institute of Organic Synthesis, Riga LV-1006, Latvia*

Kitija A. Stucere – *Institute of Solid State Physics, University of Latvia, LV-1063 Riga, Latvia*

Aivars Vembris – *Institute of Solid State Physics, University of Latvia, LV-1063 Riga, Latvia*

Glib Baryshnikov – *Laboratory of Organic Electronics, Department of Science and Technology, Linköping University, SE-60174 Norrköping, Sweden;* orcid.org/0000-0002-0716-3385

Hans Ågren – *Department of Physics and Astronomy, Uppsala University, SE-751 20 Uppsala, Sweden;* orcid.org/0000-0002-1763-9383

Jhao-Cheng Lu – *Department of Electrical Engineering, Yuan Ze University, Chungli 32003, Taiwan*

Wei-Han Lin – *Department of Electrical Engineering, Yuan Ze University, Chungli 32003, Taiwan*

Complete contact information is available at: https://pubs.acs.org/10.1021/acsami.2c00847

Notes

The authors declare no competing financial interest.

■ ACKNOWLEDGMENTS

This research was funded by the Latvian Council of Science, project No. lzp-2019/1-0231. G.B. acknowledges the financial support of the Swedish Research Council (Starting Grant No. 2020-04600). The quantum-chemical calculations were per-

formed with computational resources provided by the Swedish National Infrastructure for Computing (SNIC 2021-3-22) at the High-Performance Computing Center North (HPC2N) partially funded by the Swedish Research Council through Grant Agreement No. 2018-05973. C.-H.C. acknowledges financial support from the Ministry of Science and Technology of Taiwan (Grant Nos. 110-2221-E-155-036 and 110-2221-E-155-033-MY2).

REFERENCES

(1) Chen, H.-W.; Lee, J.-H.; Lin, B.-Y.; Chen, S.; Wu, S.-T. Liquid Crystal Display and Organic Light-Emitting Diode Display: Present Status and Future Perspectives. *Light Sci. Appl.* **2018**, *7* (3), 17168−17168.

(2) Yin, Y.; Ali, M. U.; Xie, W.; Yang, H.; Meng, H. Evolution of White Organic Light-Emitting Devices: From Academic Research to Lighting and Display Applications. *Mater. Chem. Front.* **2019**, *3* (6), 970−1031.

(3) Yersin, H.; Rausch, A. F.; Czerwieniec, R.; Hofbeck, T.; Fischer, T. The Triplet State of Organo-Transition Metal Compounds. Triplet Harvesting and Singlet Harvesting for Efficient OLEDs. *Coord. Chem. Rev.* **2011**, *255* (21−22), 2622−2652.

(4) Lamansky, S.; Djurovich, P.; Murphy, D.; Abdel-Razzaq, F.; Lee, H.-E.; Adachi, C.; Burrows, P. E.; Forrest, S. R.; Thompson, M. E. Highly Phosphorescent Bis-Cyclometalated Iridium Complexes: Synthesis, Photophysical Characterization, and Use in Organic Light Emitting Diodes. *J. Am. Chem. Soc.* **2001**, *123* (18), 4304−4312.

(5) Sotoyama, W.; Satoh, T.; Sawatari, N.; Inoue, H. Efficient Organic Light-Emitting Diodes with Phosphorescent Platinum Complexes Containing N∧C∧N-Coordinating Tridentate Ligand. *Appl. Phys. Lett.* **2005**, *86* (15), 153505.

(6) Yang, X.; Zhou, G.; Wong, W.-Y. Functionalization of Phosphorescent Emitters and Their Host Materials by Main-Group Elements for Phosphorescent Organic Light-Emitting Devices. *Chem. Soc. Rev.* **2015**, *44* (23), 8484−8575.

(7) Bizzarri, C.; Spuling, E.; Knoll, D. M.; Volz, D.; Bräse, S. Sustainable Metal Complexes for Organic Light-Emitting Diodes (OLEDs). *Coord. Chem. Rev.* **2018**, *373*, 49−82.

(8) Wenger, O. S. Photoactive Complexes with Earth-Abundant Metals. *J. Am. Chem. Soc.* **2018**, *140* (42), 13522−13533.

(9) Ma, Y.; Che, C.-M.; Chao, H.-Y.; Zhou, X.; Chan, W.-H.; Shen, J. High Luminescence Gold(I) and Copper(I) Complexes with a Triplet Excited State for Use in Light-Emitting Diodes. *Adv. Mater.* **1999**, *11* (10), 852−857.

(10) Harkins, S. B.; Peters, J. C. A Highly Emissive Cu 2 N 2 Diamond Core Complex Supported by a [PNP] - Ligand. *J. Am. Chem. Soc.* **2005**, *127* (7), 2030−2031.

(11) Chen, X.-L.; Yu, R.; Zhang, Q.-K.; Zhou, L.-J.; Wu, X.-Y.; Zhang, Q.; Lu, C.-Z. Rational Design of Strongly Blue-Emitting Cuprous Complexes with Thermally Activated Delayed Fluorescence and Application in Solution-Processed OLEDs. *Chem. Mater.* **2013**, *25* (19), 3910−3920.

(12) Hupp, B.; Schiller, C.; Lenczyk, C.; Stanoppi, M.; Edkins, K.; Lorbach, A.; Steffen, A. Synthesis, Structures, and Photophysical Properties of a Series of Rare Near-IR Emitting Copper(I) Complexes. *Inorg. Chem.* **2017**, *56* (15), 8996−9008.

(13) Hofbeck, T.; Monkowius, U.; Yersin, H. Highly Efficient Luminescence of Cu(I) Compounds: Thermally Activated Delayed Fluorescence Combined with Short-Lived Phosphorescence. *J. Am. Chem. Soc.* **2015**, *137* (1), 399−404.

(14) Leitl, M. J.; Zink, D. M.; Schinabeck, A.; Baumann, T.; Volz, D.; Yersin, H. Copper(I) Complexes for Thermally Activated Delayed Fluorescence: From Photophysical to Device Properties. *Top. Curr. Chem.* **2016**, *374* (3), 25.

(15) Linfoot, C. L.; Leitl, M. J.; Richardson, P.; Rausch, A. F.; Chepelin, O.; White, F. J.; Yersin, H.; Robertson, N. Thermally Activated Delayed Fluorescence (TADF) and Enhancing Photoluminescence Quantum Yields of [Cu I (Diimine)(Diphosphine)] + Complexes—Photophysical, Structural, and Computational Studies. *Inorg. Chem.* **2014**, *53* (20), 10854−10861.

(16) Czerwieniec, R.; Kowalski, K.; Yersin, H. Highly Efficient Thermally Activated Fluorescence of a New Rigid Cu(i) Complex [Cu(Dmp)(Phanephos)]+. *Dalt. Trans.* **2013**, *42* (27), 9826.

(17) Gómez-Suárez, A.; Nelson, D. J.; Thompson, D. G.; Cordes, D. B.; Graham, D.; Slawin, A. M. Z.; Nolan, S. P. Synthesis, Characterization and Luminescence Studies of Gold(I)−NHC Amide Complexes. *Beilstein J. Org. Chem.* **2013**, *9*, 2216−2223.

(18) Romanov, A. S.; Becker, C. R.; James, C. E.; Di, D.; Credgington, D.; Linnolahti, M.; Bochmann, M. Copper and Gold Cyclic (Alkyl)(Amino)Carbene Complexes with Sub-Microsecond Photoemissions: Structure and Substituent Effects on Redox and Luminescent Properties. *Chem. - A Eur. J.* **2017**, *23* (19), 4625−4637.

(19) Di, D.; Romanov, A. S.; Yang, L.; Richter, J. M.; Rivett, J. P. H.; Jones, S.; Thomas, T. H.; Abdi Jalebi, M.; Friend, R. H.; Linnolahti, M.; Bochmann, M.; Credgington, D. High-Performance Light-Emitting Diodes Based on Carbene-Metal-Amides. *Science (80-.)* **2017**, *356* (6334), 159−163.

(20) Hamze, R.; Peltier, J. L.; Sylvinson, D.; Jung, M.; Cardenas, J.; Haiges, R.; Soleilhavoup, M.; Jazzar, R.; Djurovich, P. I.; Bertrand, G.; Thompson, M. E. Eliminating Nonradiative Decay in Cu(I) Emitters: 99% Quantum Efficiency and Microsecond Lifetime. *Science (80-.)* **2019**, *363* (6427), 601−606.

(21) Hamze, R.; Shi, S.; Kapper, S. C.; Muthiah Ravinson, D. S.; Estergreen, L.; Jung, M.-C.; Tadle, A. C.; Haiges, R.; Djurovich, P. I.; Peltier, J. L.; Jazzar, R.; Bertrand, G.; Bradforth, S. E.; Thompson, M. E. Quick-Silver" from a Systematic Study of Highly Luminescent, Two-Coordinate, d 10 Coinage Metal Complexes. *J. Am. Chem. Soc.* **2019**, *141* (21), 8616−8626.

(22) Thompson, M. E.; Li, T. Y.; Djurovich, P.; Shlian, D. A Luminescent Two-Coordinate Au(I) Bimetallic Complex with a Tandem-Carbene Structure: A Molecular Design for the Enhancement of TADF Radiative Decay Rate. *Chem. - Eur. J.* **2021**, *27*, 6191.

(23) Romanov, A. S.; Jones, S. T. E.; Yang, L.; Conaghan, P. J.; Di, D.; Linnolahti, M.; Credgington, D.; Bochmann, M. Mononuclear Silver Complexes for Efficient Solution and Vacuum-Processed OLEDs. *Adv. Opt. Mater.* **2018**, *6* (24), 1801347.

(24) Romanov, A. S.; Yang, L.; Jones, S. T. E.; Di, D.; Morley, O. J.; Drummond, B. H.; Reponen, A. P. M.; Linnolahti, M.; Credgington, D.; Bochmann, M. Dendritic Carbene Metal Carbazole Complexes as Photoemitters for Fully Solution-Processed OLEDs. *Chem. Mater.* **2019**, *31* (10), 3613−3623.

(25) Shi, S.; Jung, M. C.; Coburn, C.; Tadle, A.; Sylvinson, M. R. D.; Djurovich, P. I.; Forrest, S. R.; Thompson, M. E. Highly Efficient Photo- and Electroluminescence from Two-Coordinate Cu(I) Complexes Featuring Nonconventional N-Heterocyclic Carbenes. *J. Am. Chem. Soc.* **2019**, *141* (8), 3576−3588.

(26) Conaghan, P. J.; Matthews, C. S. B.; Chotard, F.; Jones, S. T. E.; Greenham, N. C.; Bochmann, M.; Credgington, D.; Romanov, A. S. Highly Efficient Blue Organic Light-Emitting Diodes Based on Carbene-Metal-Amides. *Nat. Commun.* **2020**, *11* (1), 1758.

(27) Gernert, M.; Balles-Wolf, L.; Kerner, F.; Müller, U.; Schmiedel, A.; Holzapfel, M.; Marian, C. M.; Pflaum, J.; Lambert, C.; Steffen, A. Cyclic (Amino)(Aryl)Carbenes Enter the Field of Chromophore Ligands: Expanded π System Leads to Unusually Deep Red Emitting Cu I Compounds. *J. Am. Chem. Soc.* **2020**, *142* (19), 8897−8909.

(28) Conaghan, P. J.; Menke, S. M.; Romanov, A. S.; Jones, S. T. E.; Pearson, A. J.; Evans, E. W.; Bochmann, M.; Greenham, N. C.; Credgington, D. Efficient Vacuum-Processed Light-Emitting Diodes Based on Carbene−Metal−Amides. *Adv. Mater.* **2018**, *30* (35), 1802285.

(29) Feng, J.; Yang, L.; Romanov, A. S.; Ratanapreechachai, J.; Reponen, A. M.; Jones, S. T. E.; Linnolahti, M.; Hele, T. J. H.; Köhler, A.; Bässler, H.; Bochmann, M.; Credgington, D. Environmental Control of Triplet Emission in Donor−Bridge−Acceptor Organometallics. *Adv. Funct. Mater.* **2020**, *30* (9), 1908715.

(30) Romanov, A. S.; Jones, S. T. E.; Gu, Q.; Conaghan, P. J.; Drummond, B. H.; Feng, J.; Chotard, F.; Buizza, L.; Foley, M.;

https://doi.org/10.1021/acsami.2c00847
ACS Appl. Mater. Interfaces 2022, 14, 15478−15493

Linnolahti, M.; Credgington, D.; Bochmann, M. Carbene Metal Amide Photoemitters: Tailoring Conformationally Flexible Amides for Full Color Range Emissions Including White-Emitting OLED. *Chem. Sci.* **2020**, *11* (2), 435−446.
(31) Lüdtke, N.; Föller, J.; Marian, C. M. Understanding the Luminescence Properties of Cu Complexes: A Quantum Chemical Perusal. *Phys. Chem. Chem. Phys.* **2020**, *22* (41), 23530−23544.
(32) Chotard, F.; Sivchik, V.; Linnolahti, M.; Bochmann, M.; Romanov, A. S. Mono- versus Bicyclic Carbene Metal Amide Photoemitters: Which Design Leads to the Best Performance? *Chem. Mater.* **2020**, *32* (14), 6114−6122.
(33) Ying, A.; Huang, Y.-H.; Lu, C.-H.; Chen, Z.; Lee, W.-K.; Zeng, X.; Chen, T.; Cao, X.; Wu, C.-C.; Gong, S.; Yang, C. High-Efficiency Red Electroluminescence Based on a Carbene−Cu(I)−Acridine Complex. *ACS Appl. Mater. Interfaces* **2021**, *13* (11), 13478−13486.
(34) Hamze, R.; Idris, M.; Muthiah Ravinson, D. S.; Jung, M. C.; Haiges, R.; Djurovich, P. I.; Thompson, M. E. Highly Efficient Deep Blue Luminescence of 2-Coordinate Coinage Metal Complexes Bearing Bulky NHC Benzimidazolyl Carbene. *Front. Chem.* **2020**, *8*, 1.
(35) Yang, J.-G.; Song, X.-F.; Wang, J.; Li, K.; Chang, X.; Tan, L.-Y.; Liu, C.-X.; Yu, F.-H.; Cui, G.; Cheng, G.; To, W.-P.; Yang, C.; Che, C.-M.; Chen, Y. Highly Efficient Thermally Activated Delayed Fluorescence from Pyrazine-Fused Carbene Au(I) Emitters. *Chem. - Eur. J.* **2021**, *27*, 17834.
(36) Fleetham, T.; Ecton, J.; Wang, Z.; Bakken, N.; Li, J. Single-Doped White Organic Light-Emitting Device with an External Quantum Efficiency Over 20%. *Adv. Mater.* **2013**, *25* (18), 2573−2576.
(37) Cocchi, M.; Kalinowski, J.; Virgili, D.; Fattori, V.; Develay, S.; Williams, J. A. G. Single-Dopant Organic White Electrophosphorescent Diodes with Very High Efficiency and Its Reduced Current Density Roll-Off. *Appl. Phys. Lett.* **2007**, *90* (16), 163508.
(38) Piel, I.; Pawelczyk, M. D.; Hirano, K.; Fröhlich, R.; Glorius, F. A Family of Thiazolium Salt Derived N-Heterocyclic Carbenes (NHCs) for Organocatalysis: Synthesis, Investigation and Application in Cross-Benzoin Condensation. *Eur. J. Org. Chem.* **2011**, *2011* (28), 5475−5484.
(39) Li, T.; Muthiah Ravinson, D. S.; Haiges, R.; Djurovich, P. I.; Thompson, M. E. Enhancement of the Luminescent Efficiency in Carbene-Au (I) -Aryl Complexes by the Restriction of Renner−Teller Distortion and Bond Rotation. *J. Am. Chem. Soc.* **2020**, *142* (13), 6158−6172.
(40) Eng, J.; Thompson, S.; Goodwin, H.; Credgington, D.; Penfold, T. J. Competition between the Heavy Atom Effect and Vibronic Coupling in Donor−Bridge−Acceptor Organometallics. *Phys. Chem. Chem. Phys.* **2020**, *22* (8), 4659−4667.
(41) Czerwieniec, R.; Yu, J.; Yersin, H. Blue-Light Emission of Cu(I) Complexes and Singlet Harvesting. *Inorg. Chem.* **2011**, *50* (17), 8293−8301.
(42) Föller, J.; Marian, C. M. Rotationally Assisted Spin-State Inversion in Carbene−Metal−Amides Is an Artifact. *J. Phys. Chem. Lett.* **2017**, *8* (22), 5643−5647.
(43) Marcus, R. A. Electron Transfer Reactions in Chemistry. Theory and Experiment. *Rev. Mod. Phys.* **1993**, *65* (3), 599−610.
(44) O'Brien, D. F.; Baldo, M. A.; Thompson, M. E.; Forrest, S. R. Improved Energy Transfer in Electrophosphorescent Devices. *Appl. Phys. Lett.* **1999**, *74* (3), 442−444.
(45) Gong, S.; He, X.; Chen, Y.; Jiang, Z.; Zhong, C.; Ma, D.; Qin, J.; Yang, C. Simple CBP Isomers with High Triplet Energies for Highly Efficient Blue Electrophosphorescence. *J. Mater. Chem.* **2012**, *22* (7), 2894−2899.
(46) Holmes, R. J.; Forrest, S. R.; Tung, Y.-J.; Kwong, R. C.; Brown, J. J.; Garon, S.; Thompson, M. E. Blue Organic Electrophosphorescence Using Exothermic Host−Guest Energy Transfer. *Appl. Phys. Lett.* **2003**, *82* (15), 2422−2424.
(47) Xu, H.; Wang, L.-H.; Zhu, X.-H.; Yin, K.; Zhong, G.-Y.; Hou, X.-Y.; Huang, W. Application of Chelate Phosphine Oxide Ligand in Eu III Complex with Mezzo Triplet Energy Level, Highly Efficient Photoluminescent, and Electroluminescent Performances. *J. Phys. Chem. B* **2006**, *110* (7), 3023−3029.
(48) Yi, R.; Liu, G.; Luo, Y.; Wang, W.; Tsai, H.; Lin, C.; Shen, H.; Chang, C.; Lu, C. Dicyano-Imidazole: A Facile Generation of Pure Blue TADF Materials for OLEDs. *Chem. - Eur. J.* **2021**, *27* (51), 12998−13008.
(49) Ye, H.; Chen, D.; Liu, M.; Su, S.-J.; Wang, Y.-F.; Lo, C.-C.; Lien, A.; Kido, J. Pyridine-Containing Electron-Transport Materials for Highly Efficient Blue Phosphorescent OLEDs with Ultralow Operating Voltage and Reduced Efficiency Roll-Off. *Adv. Funct. Mater.* **2014**, *24* (21), 3268−3275.
(50) Wu, J.; Ameri, L.; Cao, L.; Li, J. Efficient Excimer-Based White OLEDs with Reduced Efficiency Roll-Off. *Appl. Phys. Lett.* **2021**, *118* (7), 073301.
(51) Pander, P.; Zaytsev, A. V.; Sil, A.; Williams, J. A. G.; Lanoe, P.-H.; Kozhevnikov, V. N.; Dias, F. B. The Role of Dinuclearity in Promoting Thermally Activated Delayed Fluorescence (TADF) in Cyclometallated, N∧C∧N-Coordinated Platinum Complexes. *J. Mater. Chem. C* **2021**, *9* (32), 10276−10287.
(52) Liao, J.-L.; Chi, Y.; Su, Y.-D.; Huang, H.-X.; Chang, C.-H.; Liu, S.-H.; Lee, G.-H.; Chou, P.-T. Os Metal Phosphors Bearing Tridentate 2,6-Di(Pyrazol-3-Yl)Pyridine Chelate: Synthetic Design, Characterization and Application in OLED Fabrication. *J. Mater. Chem. C* **2014**, *2* (31), 6269.
(53) Baldo, M. A.; Adachi, C.; Forrest, S. R. Transient Analysis of Organic Electrophosphorescence. II. Transient Analysis of Triplet-Triplet Annihilation. *Phys. Rev. B* **2000**, *62* (16), 10967−10977.
(54) Cho, H.; Romanov, A. S.; Bochmann, M.; Greenham, N. C.; Credgington, D. Matrix-Free Hyperfluorescent Organic Light-Emitting Diodes Based on Carbene−Metal−Amides. *Adv. Opt. Mater.* **2021**, *9* (5), 2001965.
(55) Birks, J. B. Excimers. *Rep. Prog. Phys.* **1975**, *38* (8), 903−974.
(56) Hamze, R.; Jazzar, R.; Soleilhavoup, M.; Djurovich, P. I.; Bertrand, G.; Thompson, M. E. Phosphorescent 2-, 3- and 4-Coordinate Cyclic (Alkyl)(Amino)Carbene (CAAC) Cu Complexes. *Chem. Commun.* **2017**, *53* (64), 9008−9011.
(57) Li, K.; Ming Tong, G. S.; Wan, Q.; Cheng, G.; Tong, W.-Y.; Ang, W.-H.; Kwong, W.-L.; Che, C.-M. Highly Phosphorescent Platinum Emitters: Photophysics, Materials and Biological Applications. *Chem. Sci.* **2016**, *7* (3), 1653−1673.
(58) Williams, E. L.; Haavisto, K.; Li, J.; Jabbour, G. E. Excimer-Based White Phosphorescent Organic Light-Emitting Diodes with Nearly 100% Internal Quantum Efficiency. *Adv. Mater.* **2007**, *19* (2), 197−202.
(59) Kui, S. C. F.; Chow, P. K.; Tong, G. S. M.; Lai, S.-L.; Cheng, G.; Kwok, C.-C.; Low, K.-H.; Ko, M. Y.; Che, C.-M. Robust Phosphorescent Platinum(II) Complexes Containing Tetradentate O∧N∧C∧N Ligands: Excimeric Excited State and Application in Organic White-Light-Emitting Diodes. *Chem. - Eur. J.* **2013**, *19* (1), 69−73.
(60) Li, G.; Fleetham, T.; Li, J. Efficient and Stable White Organic Light-Emitting Diodes Employing a Single Emitter. *Adv. Mater.* **2014**, *26* (18), 2931−2936.
(61) Bedford, R. B.; Betham, M. N -H Carbazole Synthesis from 2-Chloroanilines via Consecutive Amination and C−H Activation. *J. Org. Chem.* **2006**, *71* (25), 9403−9410.
(62) Sheldrick, G. M. SHELXT − Integrated Space-Group and Crystal-Structure Determination. *Acta Crystallogr. Sect. A Found. Adv.* **2015**, *71* (1), 3−8.
(63) Sheldrick, G. M. A Short History of SHELX. *Acta Crystallogr. Sect. A Found. Crystallogr.* **2008**, *64* (1), 112−122.
(64) Bourhis, L. J.; Dolomanov, O. V.; Gildea, R. J.; Howard, J. A. K.; Puschmann, H. The Anatomy of a Comprehensive Constrained, Restrained Refinement Program for the Modern Computing Environment − Olex2 Dissected. *Acta Crystallogr. Sect. A Found. Adv.* **2015**, *71* (1), 59−75.
(65) Dolomanov, O. V.; Bourhis, L. J.; Gildea, R. J.; Howard, J. A. K.; Puschmann, H. OLEX2 : A Complete Structure Solution, Refinement and Analysis Program. *J. Appl. Crystallogr.* **2009**, *42* (2), 339−341.

https://doi.org/10.1021/acsami.2c00847
ACS Appl. Mater. Interfaces 2022, 14, 15478−15493